INTERNATIONAL JOURNAL FOR NUMERICAL METHODS IN FLUIDS, VOL. 7, 653–695 (1987)

PERIODIC SOLUTIONS OF RIGID BODY–VISCOUS FLOW INTERACTION

P. G. PATTANI AND M. D. OLSON

Department of Civil Engineering, University of British Columbia, Vancouver, B.C., Canada V6T 1W5

SUMMARY

This paper describes the work on extending the finite element method to cover interactions between a viscous flow and a moving body. The problem configuration of interest is that of an arbitrarily shaped body undergoing a simple harmonic motion in an otherwise undisturbed incompressible fluid. The finite element modelling is based on a primitive variables representation of the Navier–Stokes equations using curved isoparametric elements. The non-linear boundary conditions on the moving body are obtained using Taylor series expansion to approximate the velocities at the fixed finite element grid points. The method of averaging is used to analyse the resulting periodic motion of the fluid. The stability of the periodic solutions is studied by introducing small perturbations and applying Floquet theory. Numerical results are obtained for several example body shapes and compared with published experimental results. Good agreement is obtained for the basic non-linear phenomenon of steady streaming.

KEY WORDS Fluid–Structure Interaction Incompressible Viscous Flow Finite Element Method Stability Analysis Steady Streaming

1. INTRODUCTION

Considerable research has been carried out on fluid–structure interaction problems, and today most of the analyses are handled with finite element methods. Most of this work, however, deals with inviscid fluids. A recent symposium[1] covered offshore structural applications. On the other hand, only a little work has dealt with viscous fluid applications. For example, Belytschko and Kennedy[2] and Liu[3] have both considered a general class of problems by using a mixed Eulerian–Lagrangian approach. Olson and Pattani[4,5] have developed a method to analyse the periodic flow around an oscillating body with finite amplitude.

This paper describes further work on the method and presents new results beyond those given in References 4 and 5. The problem addressed is that of an arbitrarily shaped body undergoing a simple harmonic motion in an otherwise undisturbed fluid. The finite element modelling is based on a primitive variable representation of the Navier–Stokes equations using curved isoparametric elements with quadratic interpolation for velocities and bilinear for pressure. The problem configuration is represented by a fixed finite element grid but the body moves past the grid. The non-linear boundary conditions on the moving body are obtained by expanding the relevant body boundary terms to first order in the body amplitude ratio to approximate the velocities at the finite element grid points. The method of averaging is used to analyse the resulting periodic motion of the fluid. The stability of the periodic solutions is studied by introducing small perturbations and applying Floquet theory.

Numerical results are obtained for three different body shapes, namely (1) a square body

0271–2091/87/070653–43$21.50

Received 22 May 1986
Revised 14 October 1986

oscillating parallel to one of its sides, (2) an oscillating circular body and (3) a symmetric Joukowski profile oscillating parallel to the line of symmetry. The latter case is considered to investigate the flow pattern around an asymmetrical body. In all cases, results are obtained for steady streaming, instantaneous velocity vectors in the fluid domain and stability of the flow. A comparison is made between the numerical and published experimental steady streamlines. The following is necessarily brief but more details are available in Reference 6.

2. THEORETICAL FORMULATION

2.1. Conservation equations

The problem under consideration is that of a two-dimensional body of arbitrary shape with a characteristic length b in the direction of motion, undergoing a simple harmonic motion in an otherwise still fluid (Figure 1). The motion of the body is given by $s(t) = s_0 \sin \omega t$ where s_0 is the displacement amplitude and ω the impressed frequency. The characteristic velocity in the flow is that of the body, namely $u_0 = \omega s_0$, and taking b, u_0 and ω^{-1} as co-ordinate, velocity and time-scale, respectively, the non-dimensional forms of the Navier–Stokes equations and continuity equation become

$$\frac{\partial u}{\partial t} + \beta\left(u\frac{\partial u}{\partial x} + v\frac{\partial u}{\partial y}\right) = \frac{1}{R_\omega}\left(2\frac{\partial^2 u}{\partial x^2} + \frac{\partial^2 u}{\partial y^2} + \frac{\partial^2 v}{\partial x\,\partial y} - \frac{\partial p}{\partial x}\right),$$

$$\frac{\partial v}{\partial t} + \beta\left(u\frac{\partial v}{\partial x} + v\frac{\partial v}{\partial y}\right) = \frac{1}{R_\omega}\left(\frac{\partial^2 v}{\partial x^2} + 2\frac{\partial^2 v}{\partial y^2} + \frac{\partial^2 u}{\partial x\,\partial y} - \frac{\partial p}{\partial y}\right), \tag{1}$$

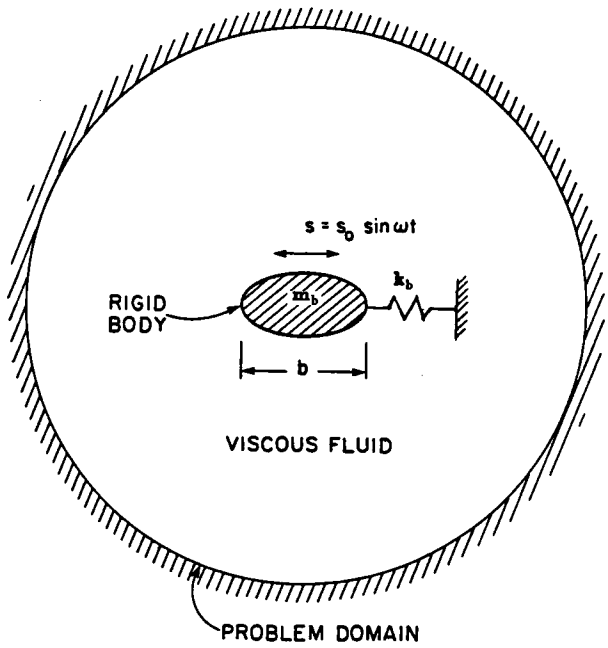

Figure 1. Problem configuration

$$\frac{\partial u}{\partial x}+\frac{\partial v}{\partial y}=0,$$

where the pressure has been non-dimensionalized with respect to the characteristic shear stress $\mu u_0/b$, μ being the fluid absolute viscosity. There are two natural Reynolds numbers in the problem, namely the usual Reynolds number and the frequency Reynolds number, given by $R_e = u_0 b/\nu$ and $R_\omega = \omega b^2/\nu$, respectively. Note that $\beta = Re/R_\omega = s_0/b$ is the body amplitude ratio.

2.2. *Moving body boundary conditions*

The body in an otherwise still fluid is describing a motion given by

$$\begin{aligned} u(s(t)) &= u(t) = u_0 \cos \omega t, \\ v(s(t)) &= v(t) = 0, \end{aligned} \tag{2}$$

where $u_0 = s_0 \omega$.

It is assumed that the finite element grid remains fixed at the mean position of the body but the body moves past the grid. To obtain velocities at the mean position of the body for any $t > 0$, we expand the relevant boundary terms by the Taylor series:

$$\begin{aligned} u(s) &= u(0) + s\left(\frac{\partial u}{\partial x}\right)_0 + \cdots \\ v(s) &= v(0) + s\left(\frac{\partial v}{\partial x}\right)_0 + \cdots \end{aligned} \tag{3}$$

where the subscript 0 indicates that the derivatives are evaluated at $s = 0$, that is at the mean position of the body.

Truncating the series at order s and substituting from $s(t) = s_0 \sin \omega t$ and equation (2) into equation (3), and rearranging, we obtain (in non-dimensional form)

$$\begin{aligned} u(0) &= \cos t - \beta\left(\frac{\partial u}{\partial x}\right)_0 \sin t, \\ v(0) &= -\beta\left(\frac{\partial v}{\partial x}\right)_0 \sin t, \end{aligned} \tag{4}$$

where all quantities are their respective non-dimensional values. The zero position in equation (4) indicates that the boundary conditions need to be applied to the finite element grid edges representing the boundary of the body in its mean position. Note that the above procedure can be applied to any description of $s(t)$ so long as $s(t)$ is small compared to the body dimension b.

It is seen from field equation (1) that β is the obvious perturbation parameter in that it governs the non-linear convection terms. Therefore, representation of the boundary condition to order β in equation (4) is consistent with the order of non-linearity in the Navier–Stokes equations.

2.3. *Finite element formulation*

The current work is based on an integrated u–v–p primitive variable representation of the Navier–Stokes equations using curved isoparametric elements with quadratic interpolation for velocities and bilinear interpolation for the pressure. Therefore,

$$\begin{aligned} u &= N_i u_i(t), \quad i = 1,2,\ldots,8 \\ v &= N_i v_i(t), \quad i = 1,2,\ldots,8 \\ p &= M_i p_i(t), \quad i = 1,\ldots,4 \end{aligned} \tag{5}$$

where u_i, v_i, p_i are time-dependent nodal variables.

Substituting equation (5) into the field equations (1) and following the Galerkin procedure over an element or equivalently following the 'restricted' variational principle[4] over an element, yields

$$\mathbf{M}\dot{\mathbf{d}} + \mathbf{K}\mathbf{d} + \beta \begin{Bmatrix} \delta^x_{ijk} u_j u_k + \delta^y_{ijk} v_j u_k \\ \delta^x_{ijk} u_j v_k + \delta^y_{ijk} v_j v_k \\ 0 \end{Bmatrix} = \mathbf{0}, \tag{6}$$

where $\mathbf{M}$ is the 'mass' matrix given by

$$\mathbf{M} = \begin{bmatrix} M^{uu}_{ij} & 0 & 0 \\ 0 & M^{vv}_{ij} & 0 \\ 0 & 0 & 0 \end{bmatrix},$$

$\mathbf{K}$ is the 'stiffness' matrix given by

$$\mathbf{K} = \frac{1}{R_\omega} \begin{bmatrix} K^{uu}_{ij} & K^{uv}_{ij} & -P^x_{ij} \\ K^{uv}_{ji} & K^{vv}_{ij} & -P^y_{ij} \\ -P^x_{ji} & -P^y_{ji} & 0 \end{bmatrix}$$

and $\mathbf{d} = \{u_j \; v_j \; p_j\}^T$ is the nodal vector of unknowns. Details of the arrays are given in Reference 4.

Substituting equation (5) into equation (4) and solving for the nodal variables at the edge of the finite element grid yields

$$\begin{aligned} u(0) &= \cos t - \beta \left(\frac{\partial N_i}{\partial x} u_i \right)_0 \sin t, \\ v(0) &= -\beta \left(\frac{\partial N_i}{\partial x} v_i \right)_0 \sin t. \end{aligned} \tag{7}$$

For each element on the boundary, as shown in Figure 2, equation (7) reduces to

$$\begin{aligned} u_i &= \cos t - \beta \sin t \, C_{ij} u_j - \beta \sin t \cos t \sum_k C_{ik}, \\ v_i &= -\beta \sin t \, C_{ij} v_j, \end{aligned} \tag{8}$$

where j is summed over the velocity variables other than those on the edge interfacing with the mean position of the body, k is summed over the velocity variables on that edge and

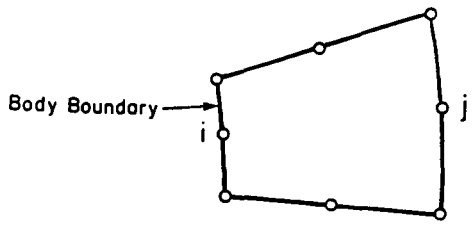

Figure 2. Body–fluid interface element

$$C_{ij} = \left(\frac{\partial N_j}{\partial x}\right)_i, \tag{9}$$

where the subscript i indicates that $\partial N_j/\partial x$ is evaluated at the location of u_i or v_i, whichever is appropriate.

When the finite element equations are assembled from equation (6), there are (say) net u and v nodal variables numbering n each and net p nodal variables numbering m. Out of these, the u and v nodal variables, each numbering r, are located on the boundary and are known from equation (8). These variables are segregated by suitable matrix manipulation and transformed to the right-hand side. This results in a matrix equation of the form

$$[\mathbf{M} + \beta \sin t\mathbf{P}]\dot{\mathbf{d}} + [\mathbf{K} + \beta \cos t\mathbf{Q} + \beta \sin t\mathbf{R}]\mathbf{d} + \beta \begin{Bmatrix} \delta^x_{ijk} u_j u_k + \delta^y_{ijk} v_j u_k \\ \delta^x_{ijk} u_j v_k + \delta^y_{ijk} v_j v_k \\ 0 \end{Bmatrix} \tag{10}$$

$$= \mathbf{F} \sin t + \mathbf{G} \cos t + \beta\{\mathbf{H} \cos^2 t + \mathbf{L} \sin t \cos t + \mathbf{J} \sin^2 t\},$$

where

$$\mathbf{d} = \{u_1 \quad u_2 \ldots u_{n-r} \quad v_1 \quad v_2 \ldots v_{n-r} \quad p_1 \quad p_2 \ldots p_m\}^{\mathrm{T}}$$

is the nodal vector of unknowns. Details of all other matrices are given in Appendix I.

2.4. *Approximate method for equations with periodic solutions*

The previous sections indicated the manner in which Navier–Stokes equations, together with boundary condition equations, are reduced to the ordinary non-linear differential equation (10). This equation still cannot be solved exactly, but approximate solutions can be obtained by the 'method of averaging' (for discussion of this technique, see Reference 7).

Let us assume that the solution of equation (10) for small β takes the form

$$\mathbf{d} = \mathbf{A} + \mathbf{B}(t) \cos t + \mathbf{C}(t) \sin t, \tag{11}$$

where $\mathbf{B}(t)$, $\mathbf{C}(t)$ are assumed to be slowly varying functions of non-dimensional time t. The first term $\mathbf{A}$ represents the steady streaming part of the solution which naturally arises for a system with quadratic non-linearities as is encountered here. From equation (11), we obtain by differentiating

$$\dot{\mathbf{d}} = -\mathbf{B}(t) \sin t + \mathbf{C}(t) \cos t + \dot{\mathbf{B}}(t) \cos t + \dot{\mathbf{C}}(t) \sin t \tag{12}$$

To obtain an autonomous system of equations governing the amplitudes $\mathbf{A}$, $\mathbf{B}(t)$, and $\mathbf{C}(t)$, equations (11) and (12) are first substituted into equation (10). Then to obtain three sets of equations for the three sets of unknowns $\mathbf{A}, \mathbf{B}(t)$ and $\mathbf{C}(t)$, the resulting equations are

(1) averaged over the period 2π
(2) multiplied by $\sin t$ and averaged over the period 2π
(3) multiplied by $\cos t$ and averaged over the period 2π.

By hypothesis, for small β, $\mathbf{B}(t)$ and $\mathbf{C}(t)$ vary much more slowly with t than t itself. Therefore $\mathbf{B}(t)$, $\mathbf{C}(t)$, $\dot{\mathbf{B}}(t)$ and $\dot{\mathbf{C}}(t)$ are considered to be constant while performing the averaging. Through this process the following equations are obtained:

$$\begin{bmatrix} 0 & 0 & \frac{\beta}{2}\mathbf{P} \\ 0 & \mathbf{M} & 0 \\ 0 & 0 & \mathbf{M} \end{bmatrix} \begin{Bmatrix} \dot{\mathbf{A}} \\ \dot{\mathbf{B}} \\ \dot{\mathbf{C}} \end{Bmatrix} + \begin{bmatrix} \mathbf{K} & \frac{\beta}{2}[\mathbf{Q} - \mathbf{P}] & \frac{\beta}{2}\mathbf{R} \\ \beta\mathbf{Q} & \mathbf{K} & \mathbf{M} \\ \beta\mathbf{R} & -\mathbf{M} & \mathbf{K} \end{bmatrix} \begin{Bmatrix} \mathbf{A} \\ \mathbf{B} \\ \mathbf{C} \end{Bmatrix}$$

$$+\beta \begin{Bmatrix} \delta^x_{ijk}(A^u_j A^u_k + B^u_j B^u_k/2 + C^u_j C^u_k/2) + \delta^y_{ijk}(A^v_j A^u_k + B^v_j B^u_k/2 + C^v_j C^u_k/2) \\ \delta^x_{ijk}(A^u_j A^v_k + B^u_j B^v_k/2 + C^u_j C^v_k/2) + \delta^y_{ijk}(A^v_j A^v_k + B^v_j B^v_k/2 + C^v_j C^v_k/2) \\ 0 \\ \delta^x_{ijk}(A^u_j B^u_k + A^u_k B^u_j) + \delta^y_{ijk}(A^v_j B^u_k + A^u_k B^v_j) \\ \delta^x_{ijk}(A^u_j B^v_k + A^v_k B^u_j) + \delta^y_{ijk}(A^v_j B^v_k + A^v_k B^v_j) \\ 0 \\ \delta^x_{ijk}(A^u_j C^u_k + A^u_k C^u_j) + \delta^y_{ijk}(A^v_j C^u_k + A^u_k C^v_j) \\ \delta^x_{ijk}(A^u_j C^v_k + A^u_k C^u_j) + \delta^y_{ijk}(A^v_j C^u_k + A^u_k C^v_j) \\ 0 \end{Bmatrix}$$

$$= \begin{Bmatrix} \frac{\beta}{2}\{\mathbf{H} + \mathbf{J}\} \\ \mathbf{G} \\ \mathbf{F} \end{Bmatrix} \tag{13}$$

where

$$\mathbf{A} = \{A^u_j \quad A^v_j \quad A^p_j\}^{\mathrm{T}},$$
$$\mathbf{B} = \{B^u_j \quad B^v_j \quad B^p_j\}^{\mathrm{T}}$$

and

$$\mathbf{C} = \{C^u_j \quad C^v_j \quad C^p_j\}^{\mathrm{T}}$$

are average values (over one period) of $\mathbf{A}$, $\mathbf{B}(t)$ and $\mathbf{C}(t)$. Here the superscripts u, v, p indicate that the amplitudes are associated with u, v, p variables, respectively. Note that $\dot{\mathbf{A}} \equiv \mathbf{0}$ by definition.

The steady-state solution corresponds to the singular points of the autonomous system of equation (13), that is when $\dot{\mathbf{B}} = \dot{\mathbf{C}} = 0$. This results in a set of non-linear algebraic equations for $\mathbf{A}, \mathbf{B}, \mathbf{C}$. These equations are solved using a Newton–Raphson procedure.

2.5. *Determination of streamlines for steady part of the solution*

The $\mathbf{A}$ component of the solution in equation (11) represents the steady flow part of the solution which has been referred to as the streaming flow in classical fluid mechanics.[8] It is possible to obtain the stream function Ψ for this steady flow simply by solving the Poisson's equation

$$\nabla^2 \Psi = \zeta = \frac{\partial u}{\partial y} - \frac{\partial v}{\partial x}, \tag{14}$$

where u, v are the steady flow components of the velocities and ζ is the steady flow component of the vorticity. Equation (14) is represented by the functional

$$I = \int\int_{\Omega} \left\{ \frac{1}{2}\left[\left(\frac{\partial \Psi}{\partial x}\right)^2 + \left(\frac{\partial \Psi}{\partial y}\right)^2 \right] - \zeta \Psi \right\} \mathrm{d}\mathbf{A} - \int_{C_s} g(s)\Psi \, \mathrm{d}s, \tag{15}$$

where Ω is the domain of the problem and $g(s) = \partial \Psi / \partial n$ is the tangential velocity specified on the natural part of the boundary C_s. In this work we use the same finite element interpolation as used for the velocities in section 2.3, and also the same finite element grid.

2.6. Stability of steady-state solutions

In previous sections an approximate steady-state solution of equation (6) was obtained using the method of averaging. This steady-state solution from equation (13) may be written as

$$\bar{\mathbf{d}} = \{\bar{u}_j \quad \bar{v}_j \quad \bar{p}_j\}^{\mathrm{T}} = \mathbf{A} + \mathbf{B}\cos t + \mathbf{C}\sin t. \tag{16}$$

Once the steady-state solution is calculated, its stability is usually investigated by superimposing a small perturbation

$$\boldsymbol{\varepsilon} = \{\varepsilon_{u_j} \quad \varepsilon_{v_j} \quad \varepsilon_{p_j}\}^{\mathrm{T}}$$

on $\bar{\mathbf{d}}$, that is by letting

$$\mathbf{d} = \bar{\mathbf{d}} + \varepsilon, \tag{17}$$

where the subscripts u_j, v_j, p_j designate perturbations to the u_j, v_j, p_j variables, respectively. Substituting equation (17) into equation (6), using the fact that $\bar{\mathbf{d}}$ is the steady-state solution of equation (6) and linearizing the equations in $\boldsymbol{\varepsilon}$, we obtain

$$\mathbf{M}\dot{\boldsymbol{\varepsilon}} + \mathbf{Z}(t)\boldsymbol{\varepsilon} = \mathbf{0} \tag{18}$$

where $\mathbf{Z}(t)$ is a time-dependent periodic matrix, that is $\mathbf{Z}(t) = \mathbf{Z}(t + 2\pi)$. The details of $\mathbf{Z}(t)$ are given in Appendix II.

The boundary conditions to be applied are $\varepsilon_{u_j}, \varepsilon_{v_j} = 0$ on the outer boundary Γ_u as well as at the mean position of the moving body.

2.7. Floquet theory

Floquet theory is used for characterizing the functional behaviour of a system of linear ordinary differential equations with periodic coefficients as in equation (18).[9]

For the system in equation (18), it is possible to define a fundamental set of solutions

$$\boldsymbol{\varepsilon}_1, \boldsymbol{\varepsilon}_2, \ldots, \boldsymbol{\varepsilon}_N,$$

where N is the order of matrices in equation (18) after applying the boundary conditions. This fundamental set of solutions can be expressed in the form of an $N \times N$ matrix $[\boldsymbol{\varepsilon}]$:

$$[\boldsymbol{\varepsilon}] = [\boldsymbol{\varepsilon}_1 \quad \boldsymbol{\varepsilon}_2 \ldots \boldsymbol{\varepsilon}_N]. \tag{19}$$

It is clear that $[\boldsymbol{\varepsilon}]$ satisfies the matrix equation

$$\mathbf{M}[\dot{\boldsymbol{\varepsilon}}] + \mathbf{Z}(t)[\boldsymbol{\varepsilon}] = \mathbf{0}. \tag{20}$$

Since $\mathbf{Z}(t) = \mathbf{Z}(t + 2\pi)$,

$$\mathbf{M}[\dot{\boldsymbol{\varepsilon}}(t + 2\pi)] + \mathbf{Z}(t + 2\pi)[\boldsymbol{\varepsilon}(t + 2\pi)] = \mathbf{M}[\dot{\boldsymbol{\varepsilon}}(t + 2\pi)] + \mathbf{Z}(t)[\boldsymbol{\varepsilon}(t + 2\pi)] = \mathbf{0}, \tag{21}$$

from which it follows that $[\boldsymbol{\varepsilon}(t + 2\pi)]$ is also a fundamental set of solutions. Hence it is related to $[\boldsymbol{\varepsilon}(t)]$ by

$$[\boldsymbol{\varepsilon}(t + 2\pi)] = \boldsymbol{\Phi}[\boldsymbol{\varepsilon}(t)], \tag{22}$$

where $\boldsymbol{\Phi}$ is a non-singular constant $N \times N$ matrix called the 'transition matrix'.

Introducing a transformation

$$[\boldsymbol{\gamma}(t)] = \boldsymbol{\Psi}[\boldsymbol{\varepsilon}(t)], \tag{23}$$

where $\mathbf{\Psi}$ is a non-singular constant $N \times N$ matrix, equation (22) can be expressed as

$$[\gamma(t+2\pi)] = \mathbf{\Psi}^{-1}\mathbf{\Phi}\mathbf{\Psi}[\gamma(t)] = \mathbf{\Upsilon}[\gamma(t)]. \tag{24}$$

The matrix $\mathbf{\Psi}$ can be chosen so that the matrix $\mathbf{\Upsilon}$ has a 'Jordan canonical form'. This form depends on the eigenvalues of $\mathbf{\Phi}$ which are the N roots of the characteristic equation

$$|\mathbf{\Phi} - \lambda[\mathbf{I}]| = 0. \tag{25}$$

When the roots of equation (25) are distinct, then the Jordan canonical form of $\mathbf{\Upsilon}$ is a diagonal matrix given by

$$\mathbf{\Upsilon} = \begin{bmatrix} \lambda_1 & 0 & 0 & \dots & 0 \\ 0 & \lambda_2 & 0 & \dots & 0 \\ 0 & 0 & \lambda_3 & \dots & 0 \\ \vdots & \vdots & \vdots & \ddots & \vdots \\ 0 & 0 & 0 & \dots & \lambda_N \end{bmatrix}. \tag{26}$$

Consequently, writing equation (24) in component form, it follows that

$$\gamma_i(t+2\pi) = \lambda_i \gamma_i(t) \quad \text{for} \quad i = 1, 2, \dots, N. \tag{27}$$

It follows from equation (27) that

$$\gamma_i(t+n2\pi) = \lambda_i^n \gamma_i(t), \tag{28}$$

where n is an integer. As $t \to \infty$ (i.e. $n \to \infty$), it follows from equation (28) that

$$\gamma_i(t) \to \begin{cases} 0, & \text{if } |\lambda_i| < 1, \\ \infty, & \text{if } |\lambda_i| > 1. \end{cases} \tag{29}$$

From equation (28) it also follows that if $\lambda_i = 1$, γ_i is periodic with period 2π, whereas if $\lambda_i = -1$, γ_i is periodic with period 4π. Therefore, stability of the steady state solution requires that

$$\lambda_{\mathbf{R}_i}^2 + \lambda_{\mathbf{I}_i}^2 \leqslant 1, \tag{30}$$

where $\lambda_{\mathbf{R}_i}$ and $\lambda_{\mathbf{I}_i}$ are the real and imaginary parts of λ_i, that is $\lambda_i = \lambda_{\mathbf{R}_i} + \mathrm{i}\lambda_{\mathbf{I}_i}$.

The boundedness criterion of equation (29) applies even when roots λ_i of equation (25) are not distinct. For further information about this and a Jordan canonical form of $\mathbf{\Upsilon}$ when the roots λ_i of equation (25) are not distinct, the reader is referred to Reference 9.

2.8. Numerical determination of the transition matrix

Friedmann, Hammond and Woo[10] have suggested an efficient numerical integration scheme which yields the transition matrix $\mathbf{\Phi}$ in a single pass without resorting to the application of initial conditions. Their integration scheme is based upon the fourth order Runge–Kutta scheme with Gill coefficients.

In the present study a similar scheme is developed, but based on the trapezoidal rule integration scheme. An implicit integration scheme was necessary here since the matrix $\mathbf{M}$ in equation (20) is a singular matrix. The trapezoidal rule is chosen since it is the only member of the trapezoidal family of methods which is second-order accurate and unconditionally stable.[11]

Applying the trapezoidal rule to equation (18) yields

$$\begin{aligned} \mathbf{M}\mathbf{v}_{n+1} + \mathbf{Z}_{n+1}\boldsymbol{\varepsilon}_{n+1} &= \mathbf{0}, \\ \boldsymbol{\varepsilon}_{n+1} &= \boldsymbol{\varepsilon}_n + \Delta t \mathbf{v}_{n+0\cdot5}, \\ \mathbf{v}_{n+0\cdot5} &= 0\cdot5\mathbf{v}_n + 0\cdot5\mathbf{v}_{n+1}, \end{aligned} \tag{31}$$

where $\boldsymbol{\varepsilon}_n$ and $\mathbf{v}_n$ are approximations to $\boldsymbol{\varepsilon}(t_n)$ and $\dot{\boldsymbol{\varepsilon}}(t_n)$, respectively, $\mathbf{Z}_n = \mathbf{Z}(t_n)$ and Δt is the time step, which is assumed constant in the present circumstances. Combining equations (31), we obtain

$$[\mathbf{M} + 0\cdot5\Delta t\mathbf{Z}_{n+1}]\boldsymbol{\varepsilon}_{n+1} = [\mathbf{M} - 0\cdot5\Delta t\mathbf{Z}_n]\boldsymbol{\varepsilon}_n, \tag{32}$$

which can also be written in the form

$$\boldsymbol{\varepsilon}_{n+1} = \mathbf{D}_n\boldsymbol{\varepsilon}_n, \tag{33}$$

where the dynamic matrix

$$\mathbf{D}_n = \mathbf{D}(t_n) = [\mathbf{M} + 0\cdot5\Delta t\mathbf{Z}_{n+1}]^{-1}[\mathbf{M} - 0\cdot5\Delta t\mathbf{Z}_n].$$

Using equation (33) the following expressions can be immediately written out

$$\begin{aligned} \boldsymbol{\varepsilon}_1 &= \mathbf{D}_0\boldsymbol{\varepsilon}_0, \\ \boldsymbol{\varepsilon}_2 &= \mathbf{D}_1\boldsymbol{\varepsilon}_1 = \mathbf{D}_1\mathbf{D}_0\boldsymbol{\varepsilon}_0, \\ \boldsymbol{\varepsilon}_n &= \mathbf{D}_{n-1}\mathbf{D}_{n-2}\ldots\mathbf{D}_0\boldsymbol{\varepsilon}_0. \end{aligned} \tag{34}$$

For constant step size $\Delta t = 2\pi/n$ and $t_0 = 0$ and $t_n = 2\pi$, the last of equations (34) reduces to

$$\begin{aligned} \boldsymbol{\varepsilon}(2\pi) &= \mathbf{D}(2\pi - \Delta t)\mathbf{D}(2\pi - 2\Delta t)\ldots\mathbf{D}(0)\boldsymbol{\varepsilon}(0) \\ &= \prod_{k=1}^{n} \mathbf{D}(2\pi - k\Delta t)\boldsymbol{\varepsilon}(0). \end{aligned} \tag{35}$$

Using equation (22) for any one fundamental set of solutions and for $t = 0$ gives

$$\boldsymbol{\varepsilon}(2\pi) = \boldsymbol{\Phi}\boldsymbol{\varepsilon}(0). \tag{36}$$

From equations (35) and (36) the transition matrix $\boldsymbol{\Phi}$ is given by

$$\boldsymbol{\Phi} = \prod_{k=1}^{n} \mathbf{D}(2\pi - k\Delta t), \tag{37}$$

where it is understood that the order of the product is important, i.e. the kth term must be before the $(k+1)$th term, etc.

After numerically evaluating the transition matrix using equation (37), the eigenvalues are evaluated using equation (25) and checked for the stability requirement given by equation (30) for $i = 1, 2, \ldots, N$.

3. NUMERICAL RESULTS

Numerical results are obtained for three different body shapes, namely (1) a square body oscillating parallel to one of its sides, (2) an oscillating circular body and (3) a symmetric Joukowski profile oscillating parallel to the line of symmetry. The boundary conditions for the flow situation are specified by the velocities $u = v = 0$ at the outer boundary and the velocities specified according to equation (8) at the body boundary. Since the body shapes considered are symmetric about the axis of oscillation, only half of the domain is modelled. By symmetry, the velocity $v = 0$ and the shear stress $\tau_{xy} = 0$ on the symmetry line. For a finite element scheme only kinematic

boundary conditions need to be specified and the homogeneous natural boundary conditions come out as part of the solution in the limit of grid refinement. Therefore, on the symmetry line only $v = 0$ is enforced. The pressure needs to be specified only at one location in the domain to obtain the pressure datum.

For the stability analysis, the velocity perturbation boundary conditions are given by $\varepsilon_u = \varepsilon_v = 0$ at the outer boundary and on the body boundary since the velocities are specified at these locations. Since only half of the domain is modelled, there are two cases to be investigated, namely the symmetric and antisymmetric modes of stability. The symmetric case is obtained by forcing the velocity perturbation $\varepsilon_v = 0$ on the symmetry line, and the antisymmetric case is obtained by forcing the velocity perturbation $\varepsilon_u = 0$ on the symmetry line. The pressure perturbation $\varepsilon_p = 0$ at the same locations at which the pressure has been specified.

Tatsuno[12-14] has presented excellent experimental results for oscillating bodies, and these results are used for verification of the present method. The results of Tatsuno are for the basic non-linear phenomenon of steady streaming, and are compared with the numerically obtained stream function for the steady component of the flow.

All the computer programs are implemented on a 48-megabyte Amdahl 5840 system with double accelerator at the University of British Columbia. Double precision arithmetic is used throughout. The solution of the linear algebraic equations and the matrix inversions are performed using a sparse matrix solving package called SPARSPAK (University of Waterloo).

3.1. Oscillating square body

The numerical results are obtained for a square body having sides of unity with the centroid of its area located at the origin of the x–y co-ordinate system and sides parallel to the axes. The body is performing harmonic oscillations parallel to the x-axis. Two finite element grids shown in Figure 3 are developed. In the present case the pressure distribution is symmetric; therefore the pressure is specified to be zero at two symmetric locations, namely (1) and (2) shown in Figure 3.

The finite element grid shown in Figure 3(a) is developed to perform preliminary calculations and to debug the program. The grid has 16 elements and 65 nodes. There are 121 net variables, 98 of which are for the velocities and 23 for the pressure. Out of the 121, 18 velocity variables lie on the body boundary and are known. For the flow situation, there are three types of coefficients **A**, **B**, **C**, and therefore this results in 309 variables in total. For the stability analysis, the total number of variables is 103. The results from this coarse grid seemed to exhibit the correct trends for both the flow situation and the stability analysis, but the accuracy was rather poor.

The finite element grid shown in Figure 3(b) is developed to represent Tatsuno's experimental set-up and has $D_0/b = 30$, where D_0 is the diameter of the outer fixed cylinder. The grid has 40 elements and 147 nodes. There are 294 net variables, 242 of which are for the velocities and 52 for the pressure. Out of the 294, 34 velocity variables lie on the body boundary and are known. The final total number of variables is 780 for the flow problem and 260 for the stability analysis.

The numerical and experimental streamlines are shown in Figures 4, 5 and 6 for values of R_ω of 1·99, 26 and 120, respectively. In each case, the numerical results are shown for two values of the body amplitude parameter β, whereas the experimental results are for only one of these values. The numerical results are obtained by plotting 31 equally spaced contours between the maximum and minimum value of the steady stream function in the plotted domain. For each case the location and the value of the maximum stream function is tabulated in Table I. Since the body in the present case is symmetric about the y-axis, the value of the minimum steady

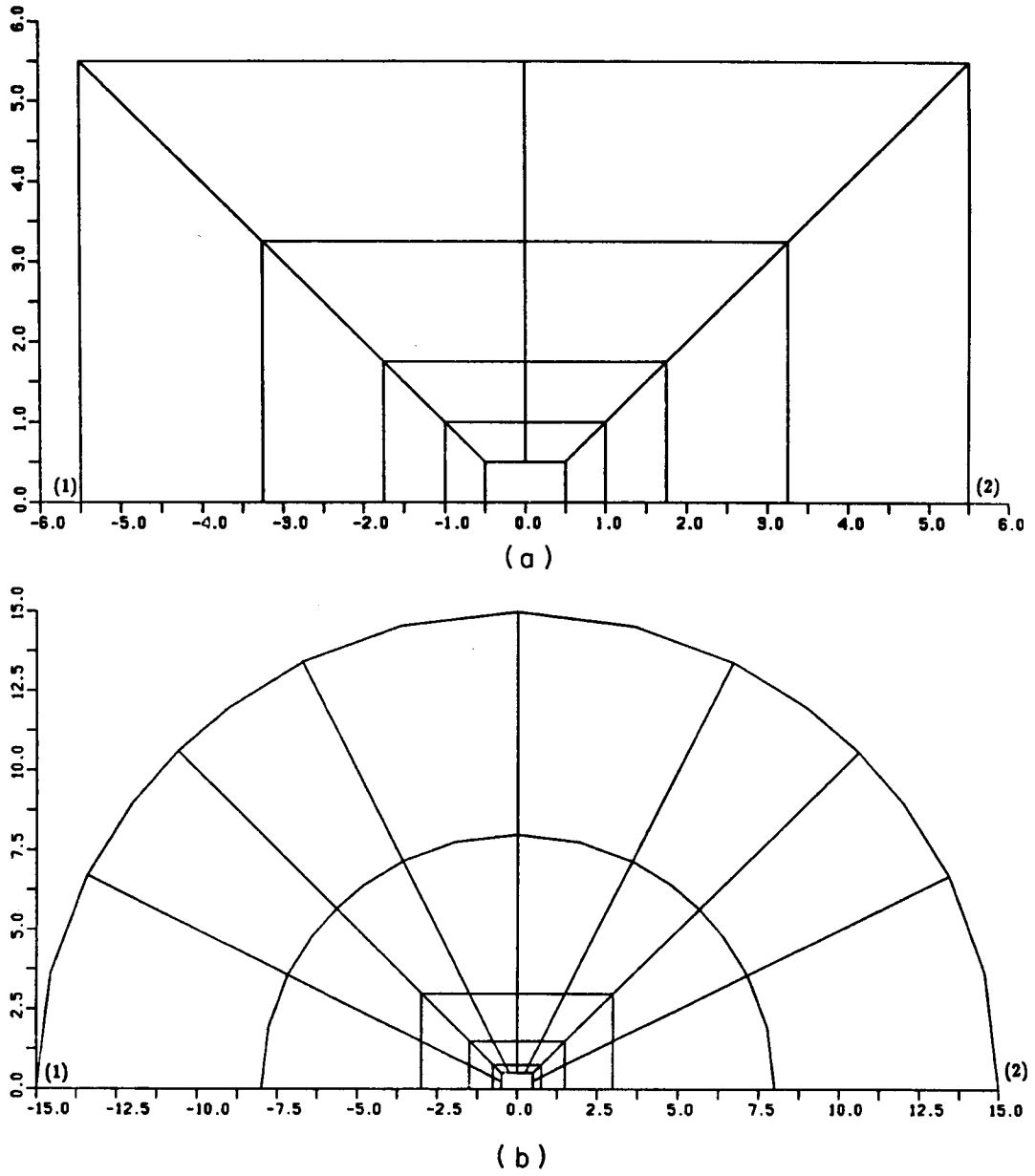

Figure 3. Finite element grids for square body

stream function is the negative of the maximum value and is located at the symmetric point about the y-axis.

Tatsuno[12] obtained his experimental pictures by a stroboscopic technique which effectively eliminated the periodic part of the flow. Tatsuno showed that there are three distinct flow regimes with different flow patterns, and these Figures show one example in each regime. The flows clearly become more complex as R_ω increases.

The example shown in Figure 4 has been classified as Type I by Tatsuno. In this type of flow

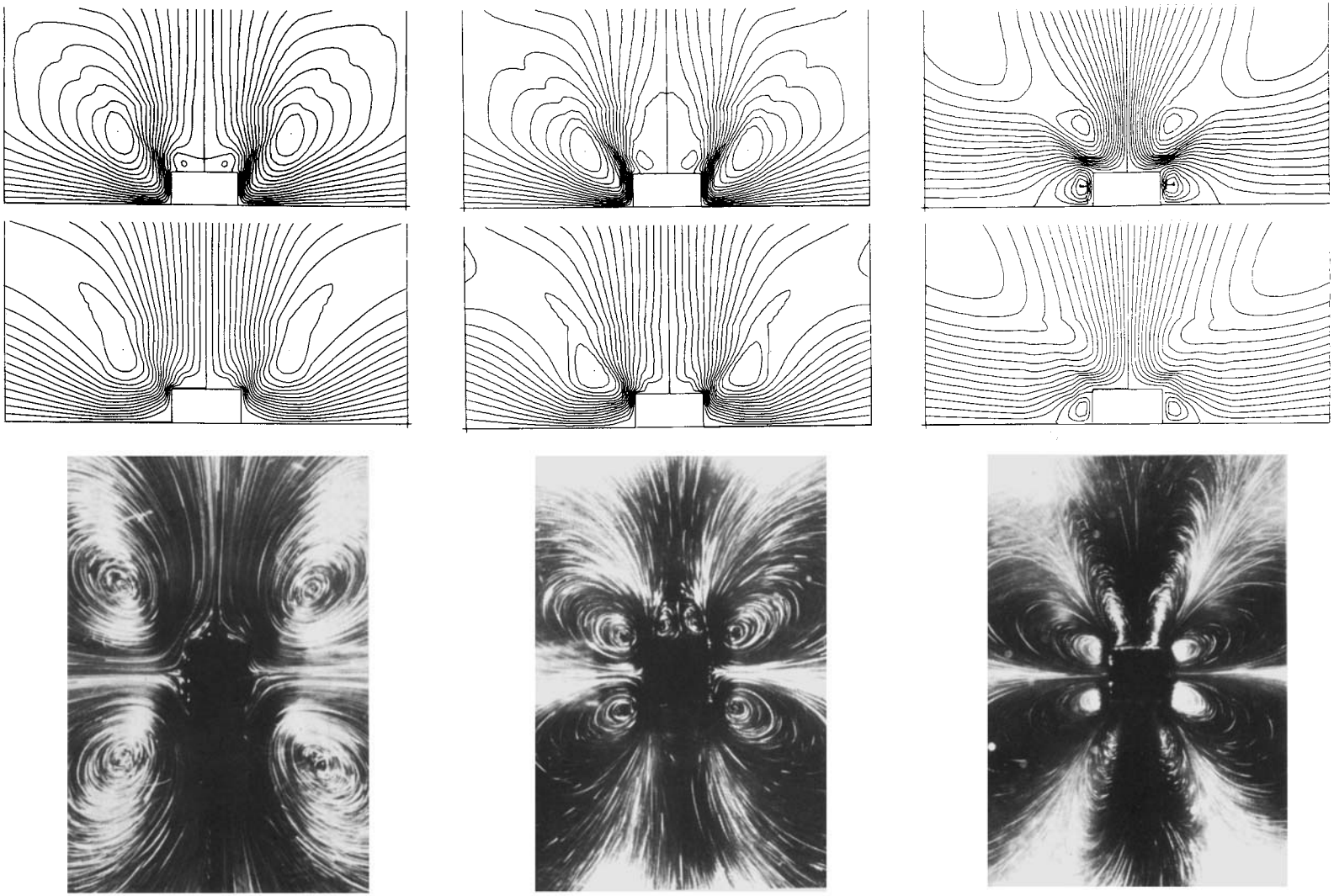

Figure 4. Steady streamlines for oscillating square body for $R_\omega = 1{\cdot}99$, $D_0/b = 30$. Top: numerical results for $\beta = 0{\cdot}1$ (upper) and $\beta = 0{\cdot}06$ (lower). Bottom: experimental results, $\beta = 0{\cdot}1$

Figure 5. Steady streamlines for oscillating square body for $R_\omega = 26$, $D_0/b = 30$. Top: numerical results for $\beta = 0{\cdot}1$ (upper) and $\beta = 0{\cdot}06$ (lower). Bottom: experimental results, $\beta = 0{\cdot}06$

Figure 6. Steady streamlines for oscillating square body for $R_\omega = 120$, $D_0/b = 30$. Top: numerical results for $\beta = 0{\cdot}1$ (upper) and $\beta = 0{\cdot}08$ (lower). Bottom: experimental results, $\beta = 0{\cdot}08$

Table I. Maximum steady stream function for oscillating square body

R_ω	β	Location of Maximum Stream function		Maximum steady stream function
		x	y	
1·99	0·06	1·2	1·05	0·02247
1·99	0·10	1·2564	1·0636	0·02012
26·00	0·06	1·0636	0·8218	0·03694
26·00	0·10	1·16	0·8218	0·02971
120·00	0·08	−2·7	2·5	0·05744
120·00	0·10	−2·3684	2·4164	0·02996

there is one main vortex system in each quadrant. In this case, the streaming flow does not separate at the edge of the body. The flow pattern of this vortex system is symmetric with respect to both the axis of oscillation and the axis perpendicular to it. Overall the numerical and experimental results agree very well. However, there are some small differences. In Figure 4, the experimental result, which is for $\beta = 0{\cdot}1$, compares better with the numerical result for $\beta = 0{\cdot}06$. The numerical result for $\beta = 0{\cdot}1$ shows the start of another pair of vortices above (and below by symmetry) the body which are not evident in the experimental result.

The example shown in Figure 5 has been classified as Type II by Tatsuno. In this example the flow separates from the square body at the edge and the twin vortices are generated enclosed between the primary vortex systems and the square body sides parallel to the oscillation direction. The twin vortices due to the flow separation have been observed to grow with increasing value of R_ω or the amplitude parameter β and ultimately the flow pattern shifts to that of Type III. Overall the numerical and experimental results agree very well for this case, too. However, there are some small differences. In Figure 5, the experimental result, which is for $\beta = 0{\cdot}06$, compares better with the numerical result for $\beta = 0{\cdot}1$. The numerical result for $\beta = 0{\cdot}06$ does not show the appearance of the secondary twin vortices. As the amplitude parameter β is increased to 0·1 the secondary twin vortices appear, but the location of the primary vortices remains essentially the same and this case compares better with the experimental result.

The example shown in Figure 6 has been classified as Type III by Tatsuno. There are two vortex systems close to the body in each quadrant and flow separates at the edge of the square body. Unlike the flow pattern of Type II, this example does not enclose the second set of twin vortices between the primary vortices and the sides parallel to the direction of oscillation. It has been observed that the two vortex systems in each quadrant become smaller with increasing R_ω. Overall the numerical and experimental results agree very well in this case too, though small discrepancies do appear. In Figure 6, the experimental result, which is for $\beta = 0{\cdot}08$ compares better with the numerical result for $\beta = 0{\cdot}1$. The numerical result at $\beta = 0{\cdot}08$ does not clearly show the appearance of the second set of twin vortices, but both the vortex systems are clearly visible at $\beta = 0{\cdot}1$.

The steady flow components illustrated in these Figures are called secondary flows, because they are expected to be small compared to the main periodic flow. For example, the forced single degree of freedom system with quadratic non-linearities (the same as the Navier–Stokes equation), described in Reference 9 shows the steady part of the response to be of the order of the perturbation parameter (β in the Navier–Stokes equations) compared to the primary harmonic response. The actual maximum of the resultant of the steady component of the velocities and its location

Table II. Maximum steady component of velocity of oscillating square body

R_ω	β	Location of Maximum steady velocity		$\frac{u_{max}}{u_0}$
		x	y	
1·99	0·06	0·625	0·625	0·081
1·99	0·10	0·5	0·25	0·282
26·00	0·06	0·625	0·3125	0·177
26·00	0·10	0·5	0·25	0·565
120·00	0·08	0·5	0·25	0·583
120·00	0·10	0·5	0·25	0·555

in the flow domain are shown in Table II. Since the body is symmetric about the y-axis these maximum velocities occur at two locations symmetric about the y-axis. These maximum velocities are obtained only from a check of nodal values, so they may not be the global maxima.

The steady-state solution obtained from equation (13) can be written as

$$\mathbf{d} = \{u_j \quad v_j \quad p_j\}^{\mathrm{T}} = \mathbf{A} + \mathbf{B}\cos t + \mathbf{C}\sin t. \tag{38}$$

Some of the results obtained from equation (38) are shown in Figures 7, 8 and 9 for values of R_ω of 1·99, 26 and 120, respectively. For all cases, the body amplitude parameter $\beta = 0{\cdot}1$. These Figures show velocity vectors over a uniform mesh in the vicinity of the body for $t = 0$, $\pi/4$, $\pi/2$, $3\pi/4$ and π, that is equal time steps over one half cycle of body motion. The size of each vector indicates the velocity magnitude. Note that the scale in each illustration is different.

It is clear from these Figures that there is one main vortex in the upper half of the fluid flow, and although it does move slightly from side to side it is located just above (and below by symmetry) the oscillating body. As the frequency Reynolds number R_ω increases, this vortex moves closer to the body and decreases in size, thereby increasing the velocity gradients in that region. Consequently, the boundary layer thickness is also decreased.

Picard iteration was used for solving the non-linear algebraic equations in the foregoing calculations. It seems to work reasonably well. All but one case, namely for $R_\omega = 120$ and $\beta = 0{\cdot}08$, were successful using the linear solution as the initial guess. The number of iterations required gradually increased from 4 to 10 as R_ω and β were increased. The aforementioned case for $R_\omega = 120$ and $\beta = 0{\cdot}08$ did not converge when a linear solution was used to start it. However, a converged result is obtained by using steps from $R_\omega = 26$ and $\beta = 0{\cdot}06$ to $R_\omega = 90$ and $\beta = 0{\cdot}08$ and subsequently to the desired result.

For the stability analysis the same two grids are used. Grid 3(a) has 23 pressure variables and 80 velocity variables for both the symmetric and antisymmetric modes of stability analysis. Grid 3(b) has 52 pressure variables and 208 velocity variables for both the symmetric and antisymmetric modes.

Preliminary calculations are performed using grid 3(a). The symmetric mode stability analysis is carried out for the oscillating square body for $R_\omega = 1{\cdot}99$ and $\beta = 0{\cdot}1$ and the results are presented in Table III for the top 52 eigenvalues in descending order of magnitudes. The flow situation considered here has also been observed experimentally and, therefore, it is expected to be stable. The results show that there are 46 eigenvalues (twice the number of pressure degrees of freedom) with magnitude equal to 1 and the rest are all less than 1. This, according to the

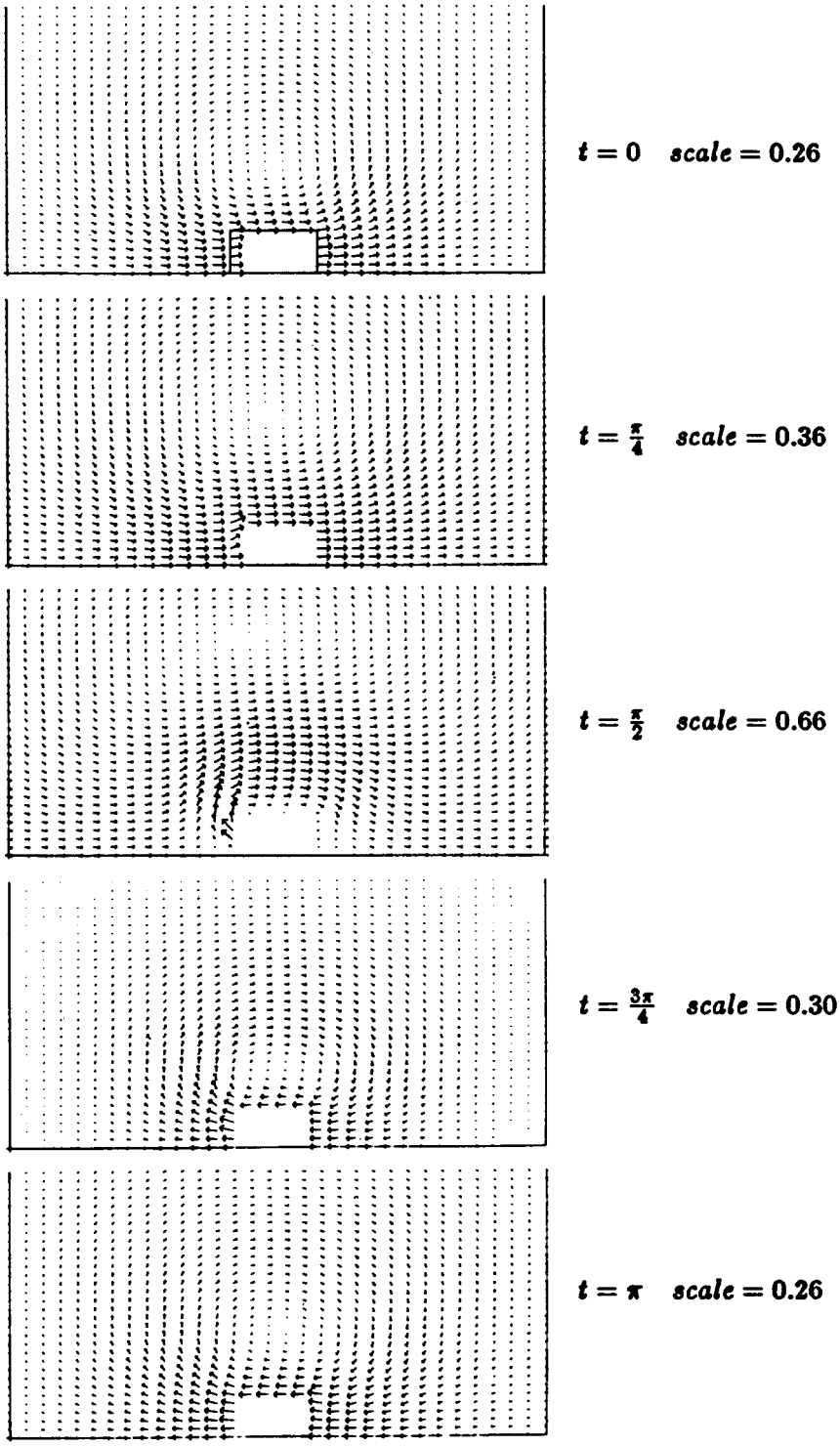

Figure 7. Velocity vectors for oscillating square body: $R_\omega = 1{\cdot}99$, $\beta = 0{\cdot}1$, $D_0/b = 30$

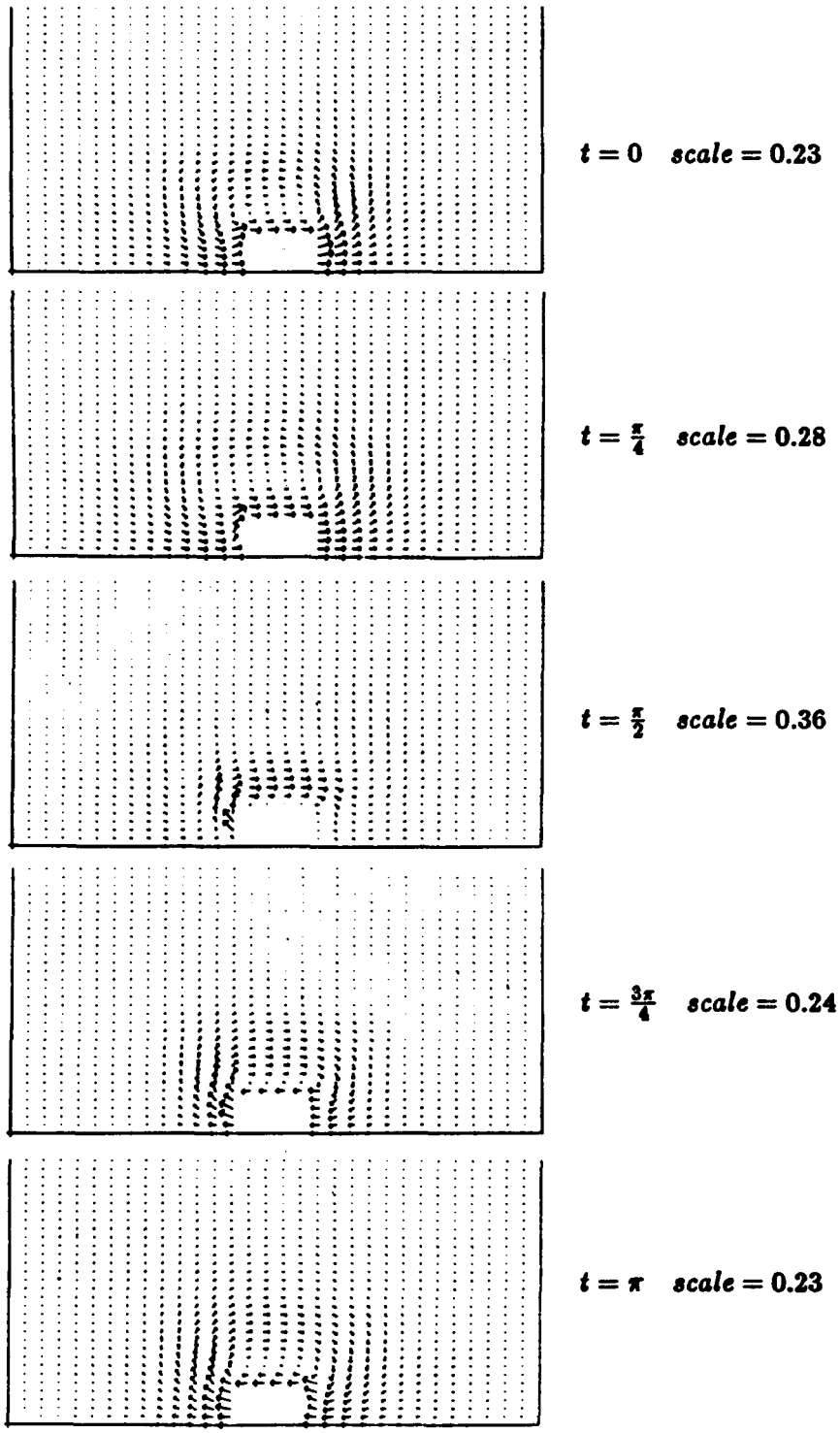

Figure 8. Velocity vectors for oscillating square body: $R_\omega = 26$, $\beta = 0{\cdot}1$, $D_0/b = 30$

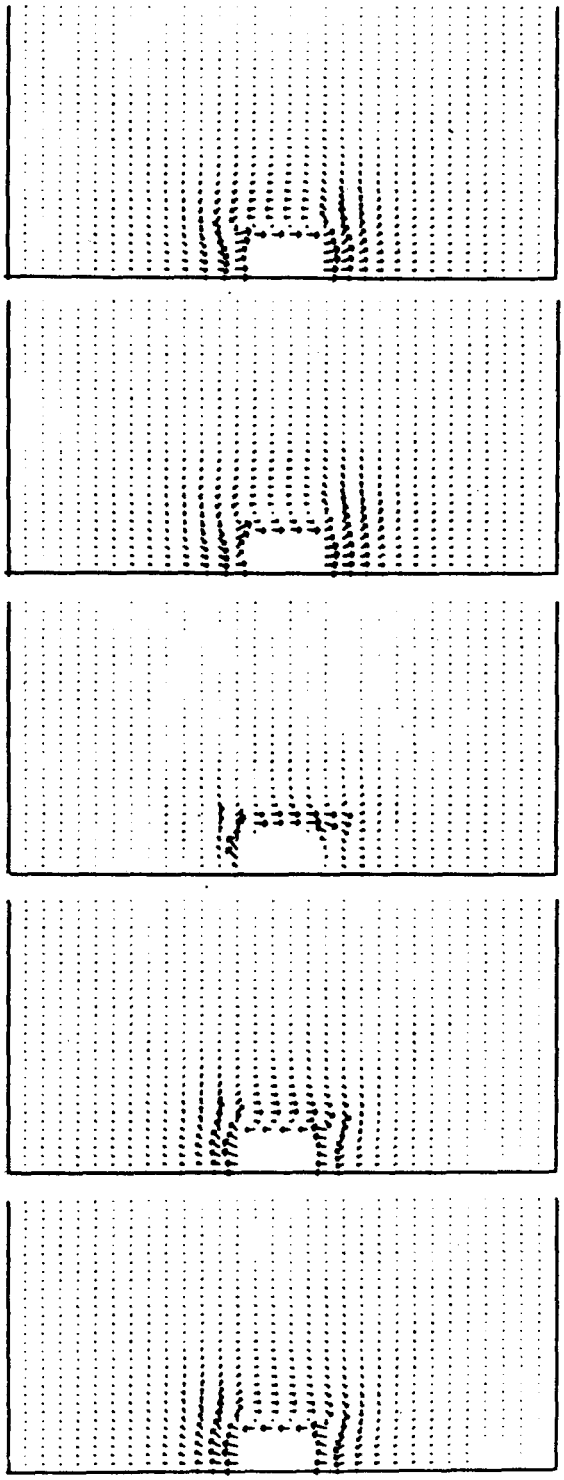

Figure 9. Velocity vectors for oscillating square body: $R_\omega = 120$, $\beta = 0{\cdot}1$, $D_0/b = 30$

Table III. Symmetric mode stability analysis for oscillating square body: $R_\omega = 1{\cdot}99$, $\beta = 0{\cdot}1$

Eigenvalue no.	Grid 3(a)					
	$\Delta t = \frac{2\pi}{5}$	$\Delta t = \frac{2\pi}{10}$	$\Delta t = \frac{2\pi}{15}$	$\Delta t = \frac{2\pi}{40}$	$\Delta t = \frac{2\pi}{45}$	$\Delta t = \frac{2\pi}{50}$
	$\lvert\lambda\rvert$	$\lvert\lambda\rvert$	$\lvert\lambda\rvert$	$\lvert\lambda\rvert$	$\lvert\lambda\rvert$	$\lvert\lambda\rvert$
1	1	1	1	1	1	1
2	1	1	1	1	1	1
3	1	1	1	1	1	1
.	.	.	.	.	.	.
.	.	.	.	.	.	.
.	.	.	.	.	.	.
46	1	1	1	1	1	1
47	0·84714	0·51039	0·22444	0·021145	0·021158	0·021167
48	0·84527	0·51492	0·22002	0·011728	0·011739	0·011747
49	0·83926	0·49601	0·20630	0·011375	0·011386	0·011394
50	0·80885	0·42786	0·14784	0·001679	0·001684	0·001687
51	0·80592	0·42170	0·14309	0·000219	0·000220	0·000221
52	0·80072	0·40445	0·13495	0·000031	0·000031	0·000031

criterion given by equation (30), indicates that the numerical steady-state solution is stable for the symmetric perturbation. As the non-dimensional time step interval Δt is reduced from $\Delta t = 2\pi/5$ to $\Delta t = 2\pi/50$, it is observed that the magnitudes of the eigenvalues (other than $|\lambda| = 1$) decrease and converge to a constant value at $\Delta t = 2\pi/40$ onwards. The converged results show that the magnitudes of the eigenvalues other than $|\lambda| = 1$ are much less than 1, qualitatively indicating that this is a 'strongly' stable situation.

The results presented in Table IV are for the same flow situation as in the previous case. However, the calculations are performed using grid 3(b) and results are presented for the top 115 eigenvalues in descending order of magnitude. The time step for convergence is expected to be much smaller for grid 3(b) as compared to the coarser grid 3(a).[10] The calculations are performed for $\Delta t = 2\pi/10$ and $\Delta t = 2\pi/40$ only, because of the large CPU time requirements. The results show that there are 104 eigenvalues (twice the number of pressure degrees of freedom) with magnitude equal to 1 and the rest are all less than 1. This indicates that the solution is stable for the symmetric perturbation. As the non-dimensional time step interval is reduced from $\Delta t = 2\pi/10$ to $\Delta t = 2\pi/40$, it is observed that the magnitude of eigenvalues (other than $|\lambda| = 1$) decreases, similarly to the previous case.

The results for the top 115 eigenvalues in descending order of magnitude are presented in Tables V and VI for the symmetric and antisymmetric perturbation modes, respectively. The flow situation considered is $R_\omega = 120$ and $\beta = 0{\cdot}1$. This flow situation is very close to the flow situation $R_\omega = 120$ and $\beta = 0{\cdot}076$, where the numerical solution did not converge. The results show that there are 104 eigenvalues (twice the number of pressure variables) with magnitude equal to 1 and the rest are all less than 1. This indicates that the solution is stable for both symmetric and antisymmetric modes. The results also show that the eigenvalues have essentially converged at $\Delta t = 2\pi/10$ and further reduction of the time step interval to $\Delta t = 2\pi/40$ brings about no change in them. Many of the eigenvalues in the present case have magnitudes close to 1, which qualitatively indicates a 'weakly' stable situation. This may be due to the fact that the flow under consideration is very close to the flow for which the steady-state solution did

Table IV. Symmetric mode stability analysis for oscillating square body: $R_\omega = 1.99$, $\beta = 0{\cdot}1$

Eigenvalue no.	Grid 3(b)	
	$\Delta t = \frac{2\pi}{10}$	$\Delta t = \frac{2\pi}{40}$
	$\lvert\lambda\rvert$	$\lvert\lambda\rvert$
1	1	1
2	1	1
3	1	1
.	.	.
.	.	.
.	.	.
104	1	1
105	0·87084	0·58450
106	0·86875	0·55128
107	0·80963	0·45520
108	0·77856	0·36658
109	0·77583	0·28828
110	0·77286	0·24335
111	0·76806	0·19939
112	0·75991	0·17017
113	0·74788	0·11284
114	0·73748	0·10934
115	0·73032	0·10521

Table V. Symmetric mode stability analysis for oscillating square body: $R_\omega = 120$, $\beta = 0{\cdot}1$

Eigenvalue no.	Grid 3(b)	
	$\Delta t = \frac{2\pi}{10}$	$\Delta t = \frac{2\pi}{40}$
	$\lvert\lambda\rvert$	$\lvert\lambda\rvert$
1	1	1
2	1	1
3	1	1
.	.	.
.	.	.
.	.	.
104	1	1
105	0·99080	0·99080
106	0·99015	0·99015
107	0·98694	0·98694
108	0·98320	0·98320
109	0·97966	0·97966
110	0·97641	0·97641
111	0·97332	0·97332
112	0·97104	0·97104
113	0·96457	0·96457
114	0·95692	0·95692
115	0·95261	0·95261

Table VI. Antisymmetric mode stability analysis for oscillating square body: $R_\omega = 120$, $\beta = 0{\cdot}1$

Eigenvalue no.	Grid 3(b)	
	$\Delta t = \frac{2\pi}{10}$	$\Delta t = \frac{2\pi}{40}$
	$\lvert\lambda\rvert$	$\lvert\lambda\rvert$
1	1	1
2	1	1
3	1	1
.	.	.
.	.	.
.	.	.
104	1	1
105	0·99605	0·99605
106	0·99007	0·99007
107	0·99005	0·99005
108	0·98724	0·98724
109	0·98592	0·98592
110	0·97984	0·97984
111	0·97664	0·97664
112	0·97421	0·97420
113	0·97182	0·97182
114	0·97014	0·97014
115	0·96493	0·96493

not converge, and therefore this may represent a bifurcation point for transition to a different flow pattern.

For all the cases considered here, the number of eigenvalues with magnitude 1 is twice the number of pressure variables. No explanation for this can be offered at this time, but it may be due to the fact that for incompressible flow the mass matrix **M** is rank deficient by the number of pressure variables because the continuity equation does not involve the pressure term explicitly.

3.2. Oscillating circular body

The numerical results are obtained for a circular body of unit diameter with its centroid located at the origin of the x–y co-ordinate system. The body is performing oscillations parallel to the x-axis. Three finite element grids, shown in Figure 10, are developed. The grids in Figures 10(a) and (b) are developed to represent Tatsuno's experimental set-up. Again the pressure is specified to be zero at two symmetric locations, namely (1) and (2) shown in Figure 10.

The three finite element grids shown in Figure 10 all have different D_0/b ratios as follows: Figures 10(a), (b) and (c) have $D_0/b = 7{\cdot}7$, $D_0/b = 15{\cdot}5$ and $D_0/b = 30$, respectively. All these grids have 48 elements and 173 nodes. There are 351 net variables, 290 for velocities and 61 for pressure. Out of the 351, 34 velocity variables lie on the body boundary and are known. The final flow problem has 951 variables and the stability analysis, 317.

The numerical and experimental steady streamlines are shown in Figures 11, 12 and 13 for values of R_ω of 3·834, 21·34 and 278·2, respectively. The numerical steady streamlines shown in Figure 14 are for $\beta = 0{\cdot}1$ and those in Figure 15 are for $R_\omega = 21{\cdot}34$.

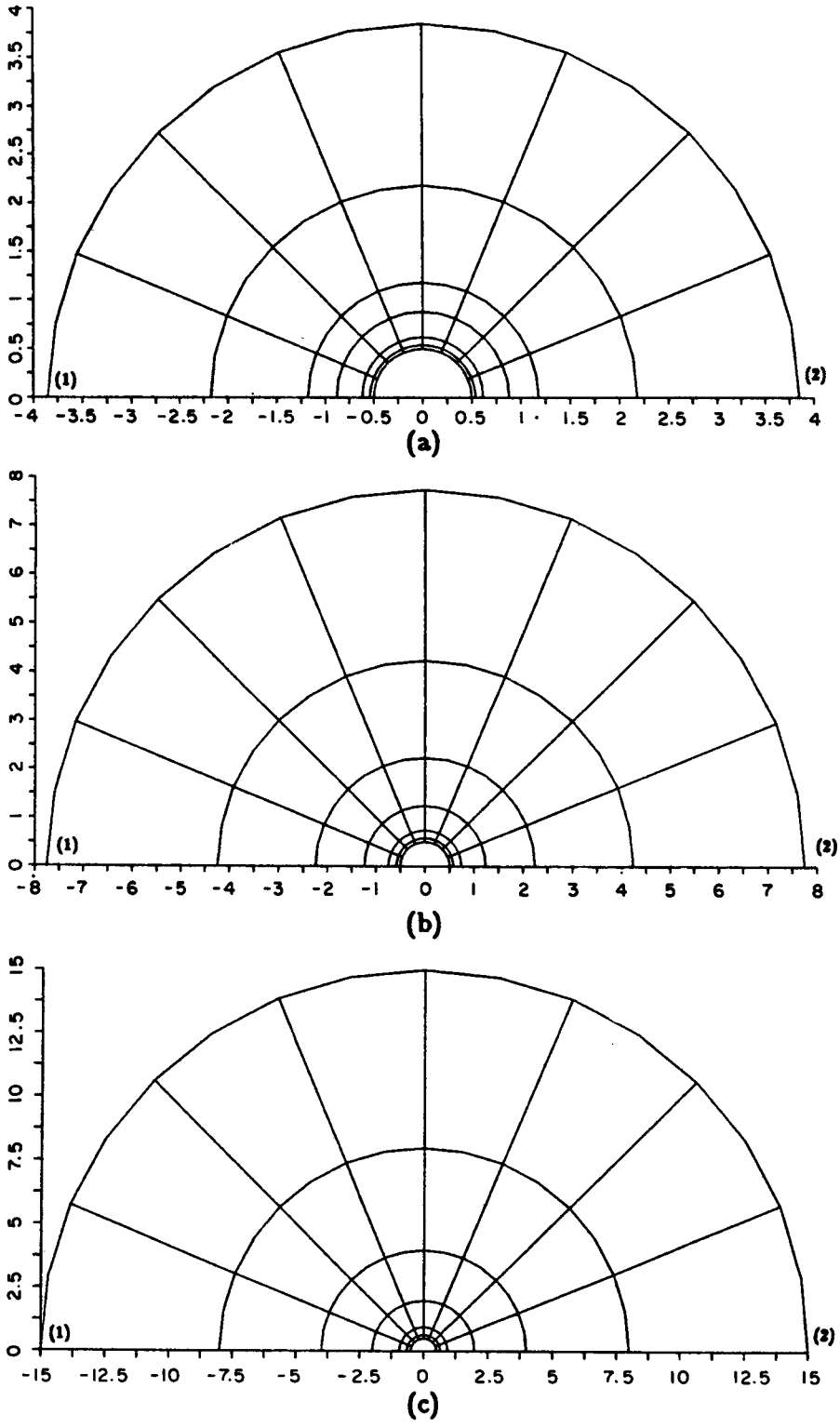

Figure 10. Finite element grids for circular body

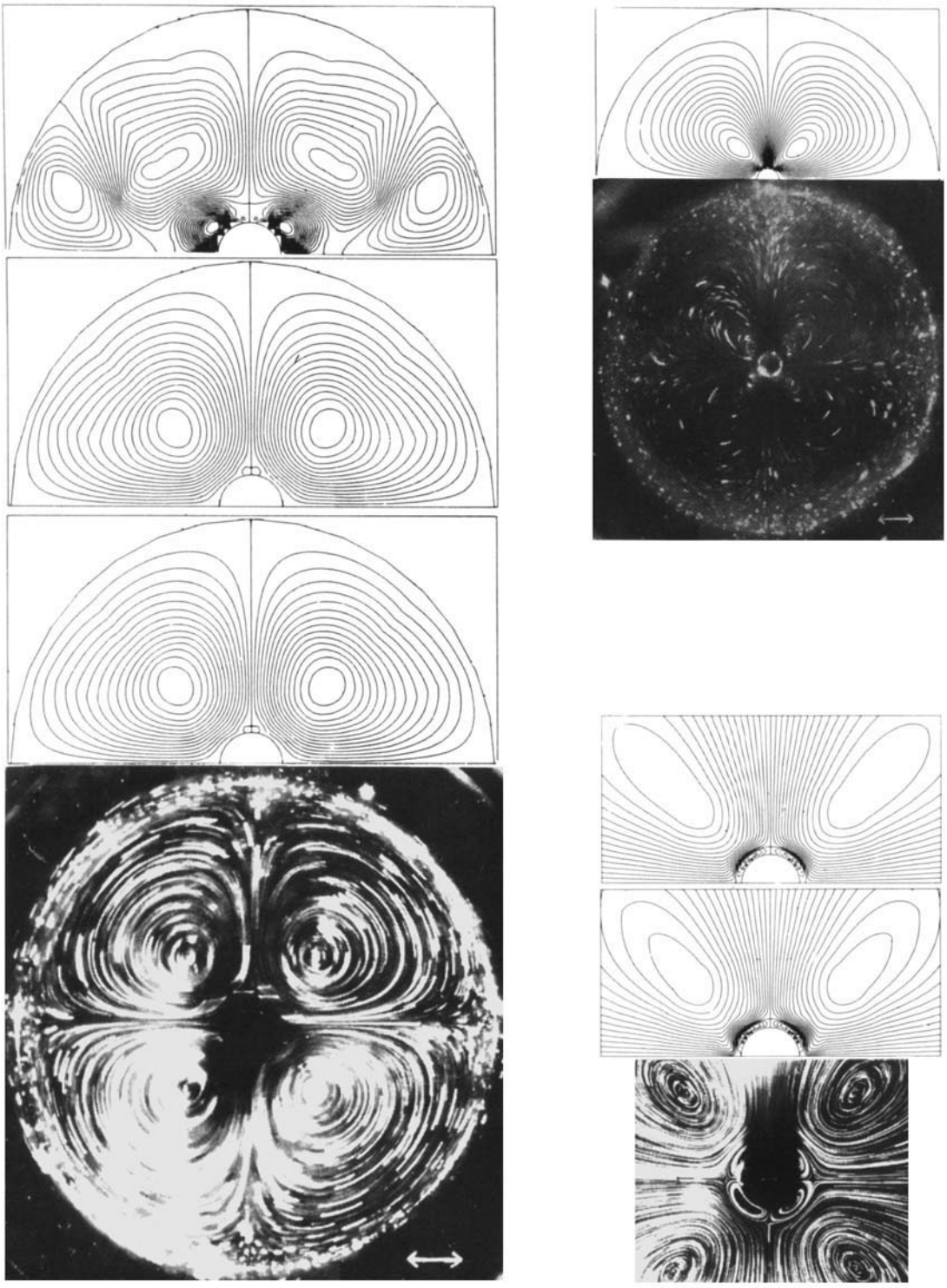

Figure 11. Steady streamlines for oscillating circular body for $R_\omega = 3{\cdot}834$, $D_0/b = 7{\cdot}7$. Top: numerical results for $\beta = 0{\cdot}161$ (upper), $\beta = 0{\cdot}13$ (middle) and $\beta = 0{\cdot}1$ (lower). Bottom: experimental results, $\beta = 0{\cdot}161$

Figure 12. Steady streamlines for oscillating circular body for $R_\omega = 21{\cdot}34$, $D_0/b = 15{\cdot}5$, $\beta = 0{\cdot}0925$

Figure 13. Steady streamlines for oscillating circular body for $R_\omega = 278{\cdot}2$, $D_0/b = 30$. Top: numerical results for $\beta = 0{\cdot}038$ (upper) and $\beta = 0{\cdot}043$ (lower). Bottom: experimental results, $\beta = 0{\cdot}046$

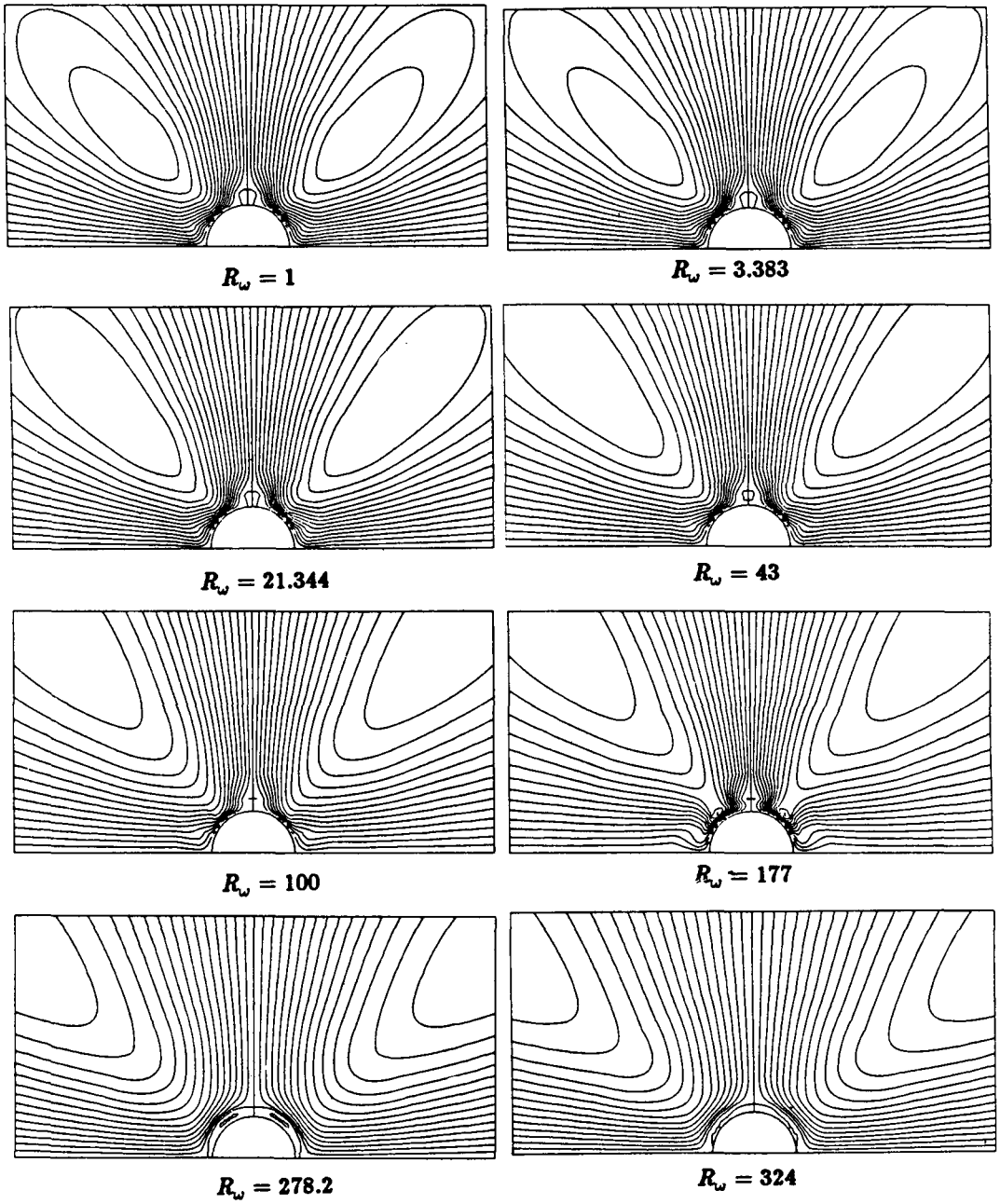

Figure 14. Steady streamlines for oscillating circular body for $\beta = 0{\cdot}1$, $D_0/b = 30$

Again 31 equally spaced contours between the maximum and the minimum values of the steady stream function are plotted. For each case, the value of D_0/b, the location of the maximum stream function and its value are presented in Table VII. Since the body in the present case is symmetric about the y-axis the value of minimum steady stream function is the negative of the maximum value and located at the corresponding symmetric point about the y-axis.

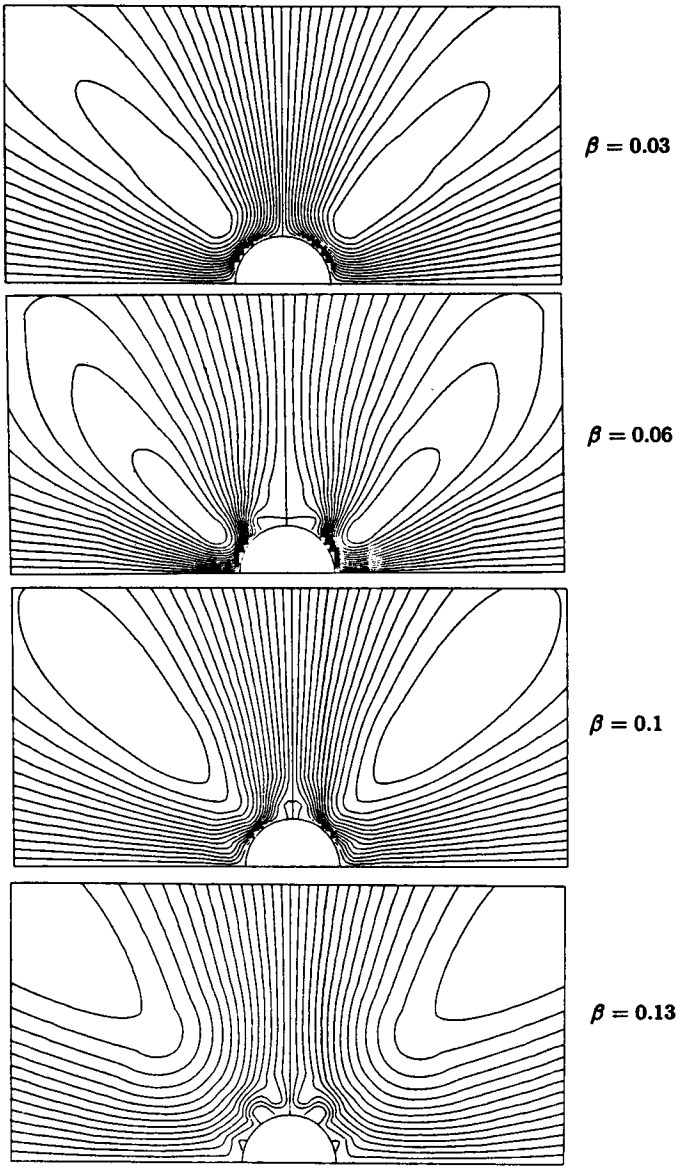

Figure 15. Steady streamlines for oscillating circular body for $R_\omega = 21{\cdot}34$, $D_0/b = 30$

Tatsuno has experimentally observed that when R_ω is less than about 64 the whole flow field in each quadrant is occupied by only one circulatory streaming vortex (the inner circulation). Also, at a critical value of the body amplitude parameter β the inner circulation shrinks down sharply and this critical value depends on R_ω.

In Figure 11 the experimental results are shown for $R_\omega = 3{\cdot}834$ and $\beta = 0{\cdot}161$, whereas the numerical results are shown for the same value of R_ω and three values of β, namely, 0·1, 0·13 and 0·161. The experimental result is for R_ω less than 64 and clearly shows the inner circulation occupying the whole flow field in each quadrant. This indicates that the critical value of β for inner

Table VII. Maximum steady stream function for oscillating circular body

R_ω	β	$\frac{D_0}{b}$	Location of maximum stream function		Maximum steady stream function
			x	y	
3·834	0·1	7·7	−0·9	0·9	0·0044
3·834	0·13	7·7	−0·9	0·9	0·0059
3·834	0·161	7·7	0·45	0·3	0·0024
21·34	0·0925	15·5	−0·45	0·525	0·0414
278·2	0·038	30	−1·3	1·3	0·0129
278·2	0·043	30	−1·3	1·25	0·0119
1	0·1	30	1·2	1·2	0·0278
3·383	0·1	30	1·2	1·2	0·0440
21·34	0·1	30	1·65	1·65	0·0798
43	0·1	30	1·95	2·025	0·0969
100	0·1	30	2·35	2·575	0·0878
177	0·1	30	2·35	2·65	0·0285
278·2	0·1	30	−2·9	2·45	0·0712
324	0·1	30	−2·9	2·325	0·1158
21·34	0·03	30	0·65	0·625	0·0088
21·34	0·06	30	0·75	0·425	0·0356
21·34	0·1	30	1·65	1·65	0·0798
21·34	0·13	30	−2·7	2·4	0·0426

circulation to shrink is greater than 0·161. The numerical results for $\beta = 0{\cdot}1$ and 0·13 show the inner circulation occupying the whole flow field in each quadrant, similarly to the experiment. The flow pattern of the inner circulation and the location of its core are very close to the experiment. But the numerical result for $\beta = 0{\cdot}161$ shows that the inner circulation has sharply shrunk. This indicates that the critical value of β is between 0·13 and 0·161. Overall, the numerical results exhibit the same phenomena as observed experimentally.

In Figure 12 the experimental and numerical results are both shown for $R_\omega = 21{\cdot}34$ and $\beta = 0{\cdot}0925$. For both cases the core of the inner circulation is closer to the cylinder than in the previous case. Nevertheless, the circulation expands over the whole flow field. The core of the inner circulation appears to be closer to the cylinder for the experimental case as compared to the numerical case. Overall, the agreement between the experimental and the numerical results is very good. For both cases, the inner circulation occupies the whole flow field in each quadrant. This indicates two things, namely (1) the value of R_ω for transition to the case where the secondary vortex system appears is greater than $R_\omega = 21{\cdot}34$, and (2) at $R_\omega = 21{\cdot}34$ the critical value of β at which the inner circulation shrinks is greater than $\beta = 0{\cdot}0925$.

In Figure 13 the experimental results are shown for $R_\omega = 278{\cdot}2$ and $\beta = 0{\cdot}046$, whereas the numerical results are shown for the same value of R_ω and two values of β, namely 0·038 and 0·043. The numerical and experimental results are for R_ω greater than 64 and both clearly show the appearance of the secondary vortices close to the body. There is very good agreement between the experimental and numerical results regarding the flow pattern on the location of both the vortices in each quadrant. However, the numerical results show the secondary vortex more tightly packed to the circular body than the experimental one. The numerical result for $\beta = 0{\cdot}046$ did not converge

even when the solution for $\beta = 0{\cdot}043$ was used as an initial guess solution. This may represent a bifurcation point close to $\beta = 0{\cdot}046$ for transition to different flow patterns. This may also be indicated by the fact that the stream function for $\beta = 0{\cdot}043$ exhibits a sharper curvature close to the horizontal stagnation points as compared to the case of $\beta = 0{\cdot}038$.

The numerical steady streamlines shown in Figure 14 are for values of β of 0·1 and R_ω of 1, 3·383, 21·34, 43, 100, 177, 278·2 and 324. The stream function results show that the core of the primary vortex system moves away from the circular body as R_ω is increased from 1 to 324. This is also indicated in Table VII, which shows that the location of the maximum value of the steady stream function moves away from the body for the present case as R_ω is increased. The numerical streamlines also show that the inner circulation occupies the whole flow field for values of R_ω of 1, 3·383, 21·34, 43 and 100. The results for values of R_ω or 177, 278·2 and 324 show the appearance of the secondary vortices close to the body. This indicates that the value of R_ω for transition to the case where the secondary vortices appear is between $R_\omega = 100$ and $R_\omega = 177$. The fact that the numerical streamlines for $R_\omega = 177$ and $\beta = 0{\cdot}03$ (not shown here) also show the appearance of secondary vortices indicates that at $R_\omega = 177$ the secondary vortices appear, irrespective of the value of β.

The numerical steady streamlines shown in Figure 15 are for values of R_ω of 31·24 and β of 0·03, 0·06, 0·1 and 0·13. The stream function results show that the inner circulation occupies the whole flow field or β of 0·03, 0·06 and 0·1. For $\beta = 0{\cdot}13$ the inner circulation has shrunk close to the body. This indicates that the critical value of β for inner circulation to shrink is between 0·1 and 0·13 for $R_\omega = 21{\cdot}34$.

The steady flow components illustrated in these Figures are expected to be small compared to the main periodic flow. The actual maximum of the resultant of the steady component of the velocities, its location in the flow domain and D_0/b ratio for which the numerical computation is performed are shown in Table VIII. Since the body is symmetric about the y-axis these maximum velocities occur at two locations symmetric about the y-axis. These maximum velocities are obtained only from a check of nodal values, and hence may not be the global maxima. In all cases the maximum velocity occurred at the body mean position.

In Table VIII the effect of change of D_0/b is shown for three flow situations, namely (1) $R_\omega = 3{\cdot}834$ and $\beta = 0{\cdot}1$,(2) $R_\omega = 3{\cdot}834$ and $\beta = 0{\cdot}161$ and (3) $R_\omega = 21{\cdot}34$ and $\beta = 0{\cdot}1$. In each case there is a change in the location and magnitude of the maximum steady velocity with a change in D_0/b. The flow pattern for the steady streaming looks essentially the same for the flow situations (1) and (3). However, some differences were observed for the flow situation (2). This may be due to a shift in the critical value of β for the inner circulation to shrink. Further investigations are necessary to examine the effect of D_0/b.

Some of the results from equation (38) for this case are shown in Figures 16, 17 and 18 for $R_\omega = 3{\cdot}834, 278{\cdot}2$ and 324, respectively. The results in Figures 16 and 18 are shown for the body amplitude parameter $\beta = 0{\cdot}1$ and the one in Figure 17 for $\beta = 0{\cdot}043$. These Figures show velocity vectors over a uniform mesh in the vicinity of the body for $t = 0, \pi/4, \pi/2$ and $3\pi/4$, that is equal time steps over one half cycle of the body motion. The size of each vector indicates the velocity magnitude.

It is clear from these Figures that there is one main vortex in the upper half of the fluid and although it does move slightly from side to side it is located just above (and below by symmetry) the oscillating body. As the frequency Reynolds number R_ω increases, this vortex moves closer to the body and decreases in size, thereby increasing the velocity gradients in that region. Consequently, the boundary layer thickness is also decreased.

A full non-linear Newton–Raphson solver with the Jacobian $[J]$ updated every alternate iteration is used for solving the non-linear algebraic equations. The converged results are obtained

Table VIII. Maximum steady component of velocity for oscillating circular body

R_ω	β	$\frac{D_0}{b}$	Location of maximum steady velocity		$\frac{u_{max}}{u_0}$
			x	y	
1	0·1	30	0·5	0	0·2859
3·834	0·1	7·7	0·0975	0·4904	0·0119
3·834	0·1	30	0·5	0	0·4942
3·834	0·13	7·7	0·0975	0·4904	0·0163
3·834	0·161	7·7	0·4904	0·0975	0·0582
3·834	0·161	30	0·3536	0·3536	0·2486
21·34	0·03	30	0·3536	0·3536	0·1010
21·34	0·06	30	0·3536	0·3536	0·7288
21·34	0·0925	15·5	0·1913	0·4619	0·4794
21·34	0·0925	30	0·5	0	1·0424
21·34	0·1	30	0·5	0	0·8141
21·34	0·13	30	0·3536	0·3636	0·6353
43	0·1	30	0·1913	0·4619	0·8819
100	0·1	30	0·1913	0·4619	0·8281
177	0·1	30	0·1913	0·4619	0·6835
278·2	0·038	30	0·3536	0·3536	0·2317
278·2	0·043	30	0·4619	0·1913	0·2587
278·2	0·1	30	0·3536	0·3536	0·5581
324	0·1	30	0·4619	0·1913	0·5678

within five iterations for all cases presented here except one. For the case of $R_\omega = 177$, $\beta = 0{\cdot}13$ and $D_0/b = 30$, eleven iterations are required when the case of $R_\omega = 3{\cdot}383$ and $\beta = 0{\cdot}03$ is used as an initial guess solution. Some cases did not converge at all. For example, for $R_\omega = 278{\cdot}2$, $\beta = 0{\cdot}0463$ and $D_0/b = 30$ the solution does not converge even when the case of $R_\omega = 278{\cdot}2$ and $\beta = 0{\cdot}043$ is used as an initial guess solution. This numerical instability may represent a bifurcation point to different flow patterns.

The results for the stability analysis are obtained by using the finite element grid in Figure 10(c) with $D_0/b = 30$. This grid has 61 pressure variables and 256 velocity variables for both the symmetric and antisymmetric modes of stability analysis.

The stability analysis is performed for the oscillating circular body for $R_\omega = 324$ and $\beta = 0{\cdot}1$. The results for the top 135 eigenvalues are presented in descending order of their magnitudes in Tables IX and X for the symmetric and antisymmetric modes, respectively. The flow situation considered here is very close to the flow situations with the same values of R_ω of 324 and β of 0·06 and 0·13, where the numerical results did not converge. The results show that there are 122 eigenvalues (twice the number of pressure degrees of freedom) with the magnitude equal to 1 and the rest are all less than 1. This, according to the criterion given by equation (30) indicates that the steady-state solution is stable for both symmetric and antisymmetric perturbations. The results also show that the eigenvalues have essentially converged at $\Delta t = 2\pi/10$ and further reduction of the time step interval to $\Delta t = 2\pi/40$ brings about no change in them. Many of the eigenvalues in the present case have magnitudes close to 1, which qualitatively indicates a 'weakly' stable situation. This may be due to the fact that the flow under consideration is very close to the flow for which a numerically converged steady-state solution was not obtained and, therefore, may represent a bifurcation point for transition to different flow patterns.

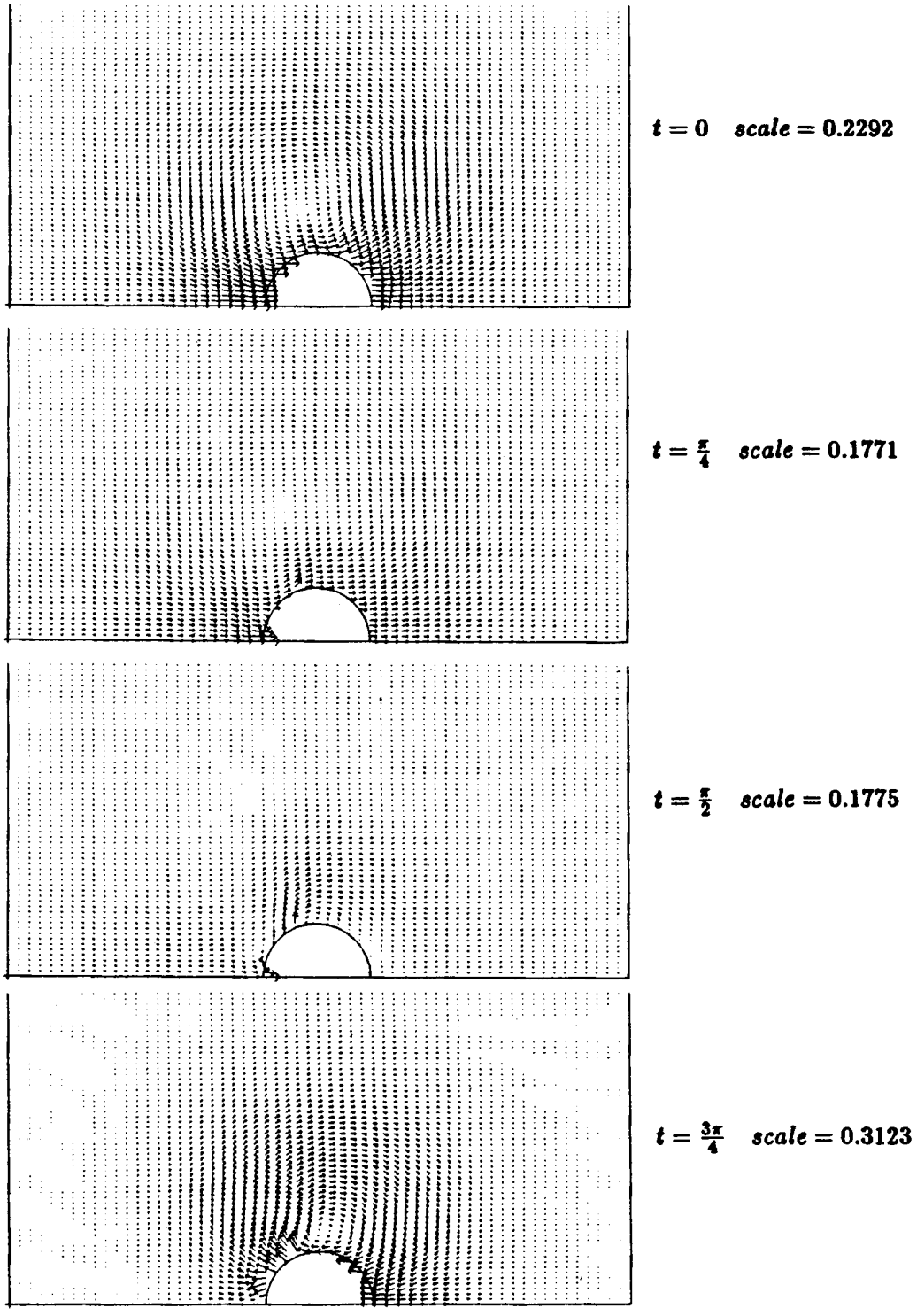

Figure 16. Velocity vectors for oscillating circular body: $R_\omega = 3{\cdot}834$, $\beta = 0{\cdot}1$, $D_0/b = 30$

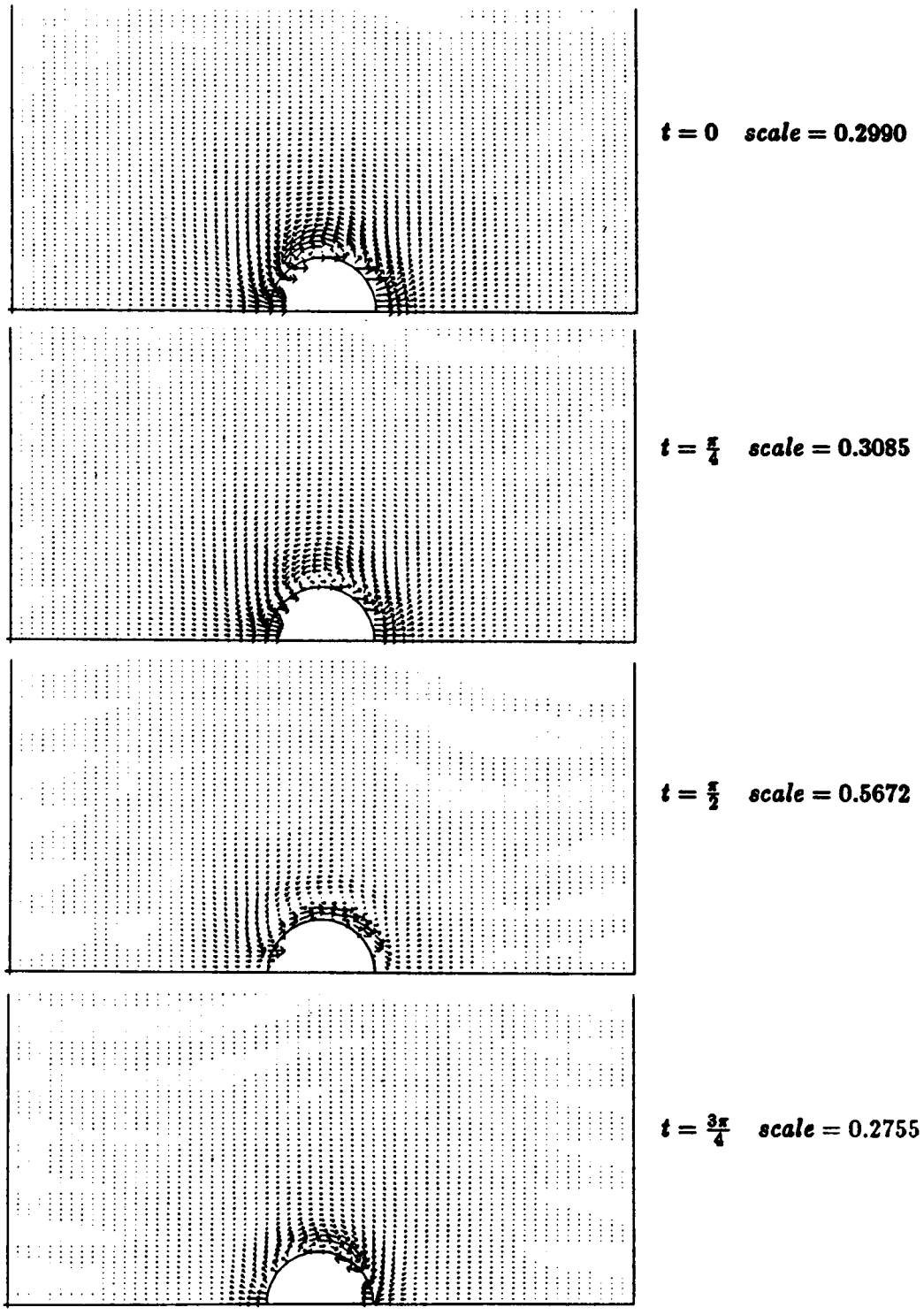

Figure 17. Velocity vectors for oscillating circular body: $R_\omega = 278{\cdot}2$, $\beta = 0{\cdot}043$, $D_0/b = 30$

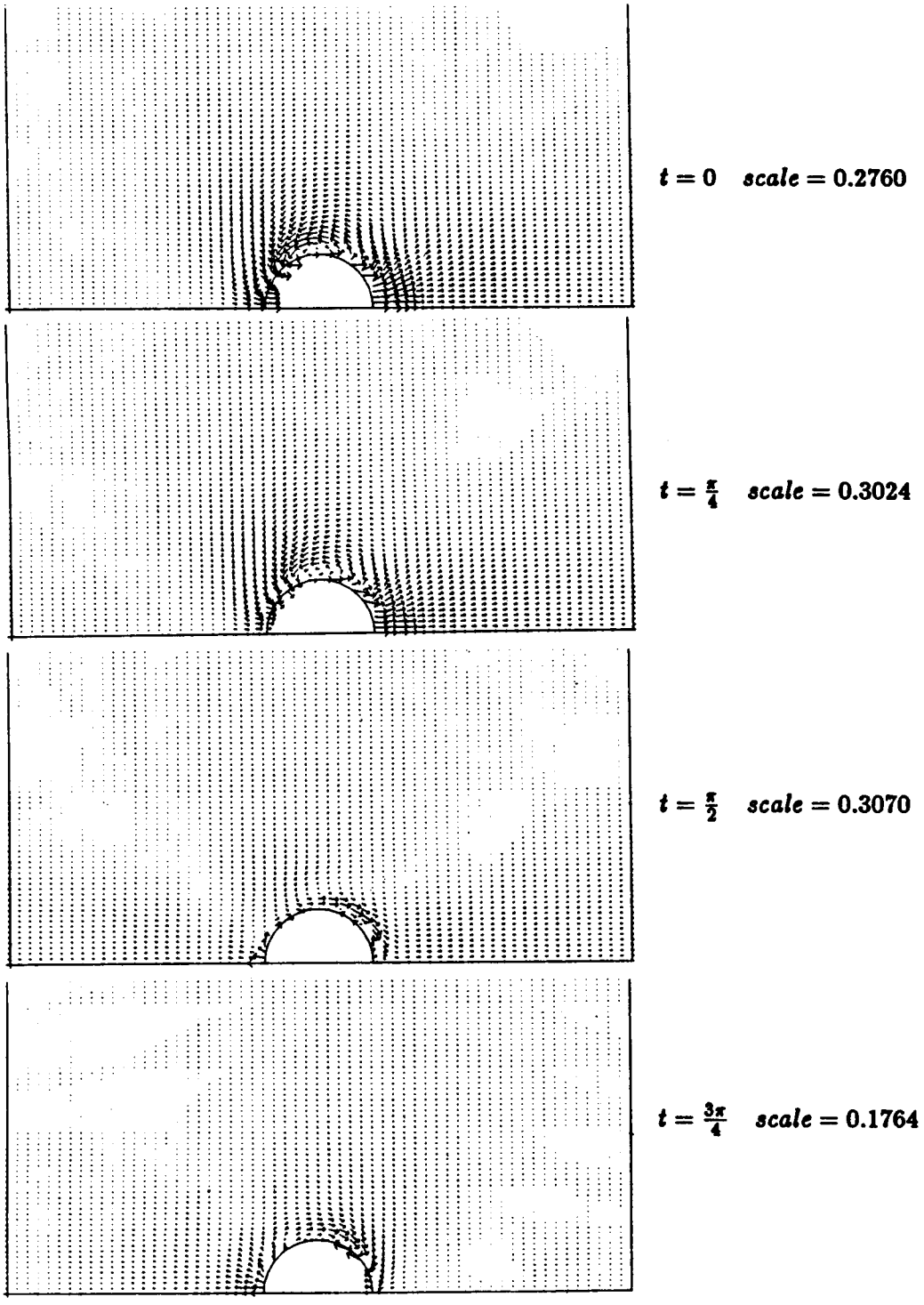

Figure 18. Velocity vectors for oscillating circular body: $R_\omega = 324$, $\beta = 0{\cdot}1$, $D_0/b = 30$

Table IX. Symmetric mode stability analysis for oscillating circular body: $R_\omega = 324$, $\beta = 0{\cdot}1$

Eigenvalue no.	$\Delta t = \frac{2\pi}{10}$	$\Delta t = \frac{2\pi}{40}$
	$\lvert\lambda\rvert$	$\lvert\lambda\rvert$
1	1	1
2	1	1
3	1	1
.	.	.
.	.	.
.	.	.
122	1	1
123	0·99597	0·99597
124	0·99594	0·99594
125	0·99372	0·99372
126	0·99147	0·99147
127	0·98686	0·98686
128	0·98472	0·98472
129	0·98353	0·98353
130	0·97974	0·97974
131	0·97941	0·97941
132	0·97645	0·97645
133	0·97352	0·97352
134	0·97244	0·97244
135	0·96951	0·96951

It should be noted that in the present case also, the number of eigenvalues with magnitude 1 is twice the number of pressure variables.

3.3. Oscillating symmetric Joukowski profile

The numerical results are obtained for a symmetric Joukowski profile of unit length. The body is performing oscillations parallel to the x-axis. The finite element grid shown in Figure 19 is developed for this case. To compare with Tatsuno's experimental set-up, this grid has $D_0/b = 18{\cdot}3$. In the present case the pressure is specified to be zero at location (1) shown in Figure 19.

The finite element grid shown in Figure 19 has 48 elements and 173 nodes. There are 352 net variables, 290 of which are for velocities and 62 for pressure. Out of the 352, 34 velocity variables lie on the body boundary and are known. The final flow problems has 954 variables, and the stability analysis, 318.

The numerical and experimental steady streamlines are shown in Figures 20 and 21 for values of R_ω of 55·1 and 206, respectively. Again 31 equally spaced contours between the maximum and minimum values of the steady stream function are plotted. For each case, the location and value of both the maximum and minimum values of the stream function are presented in Table XI.

An example of the flow at $R_\omega = 55{\cdot}1$, a relatively small value, is given in Figure 20. In this case the experimental result is for a body amplitude parameter β of 0·06 whereas the numerical results are for three values of β, namely (1) 0·1, (2) 0·06 and (3) 0·01. The flow field around the body is almost

Table X. Antisymmetric mode stability analysis for oscillating circular body: $R_\omega = 324$, $\beta = 0{\cdot}1$

Eigenvalue no.	$\Delta t = \frac{2\pi}{10}$	$\Delta t = \frac{2\pi}{40}$
	$\lvert\lambda\rvert$	$\lvert\lambda\rvert$
1	1	1
2	1	1
3	1	1
.	.	.
.	.	.
.	.	.
122	1	1
123	0·99846	0·99846
124	0·99504	0·99504
125	0·99490	0·99490
126	0·99123	0·99123
127	0·99006	0·99006
128	0·98816	0·98816
129	0·98676	0·98676
130	0·98421	0·98421
131	0·98370	0·98371
132	0·98168	0·98168
133	0·98105	0·98105
134	0·98012	0·98012
135	0·97781	0·97781

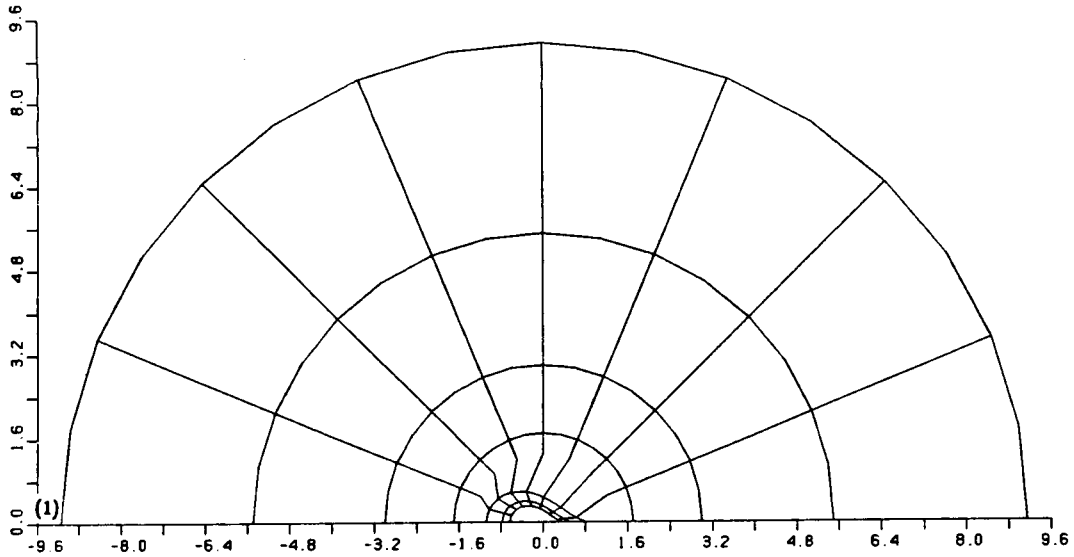

Figure 19. Finite element grid for Joukowski profile

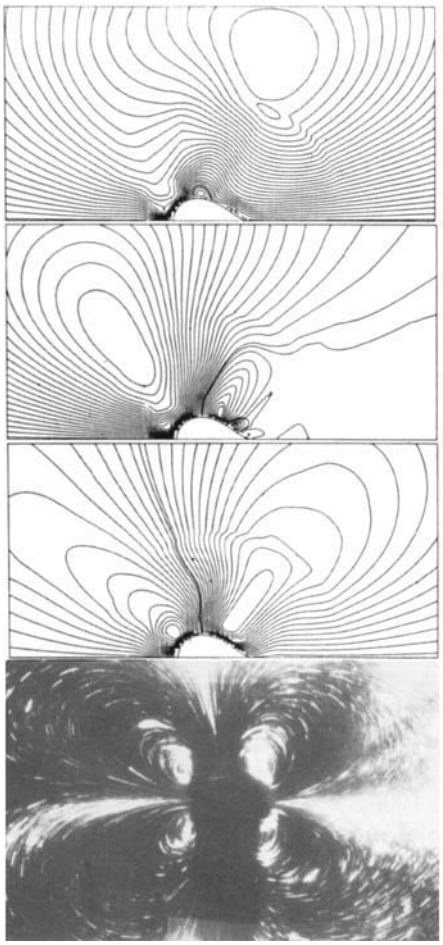

Figure 20. Steady streamlines for oscillating Joukowski profile for $R_\omega = 55{\cdot}1$, $D_0/b = 18{\cdot}3$. Top: numerical results for $\beta = 0{\cdot}1$ (upper), $\beta = 0{\cdot}06$ (middle) and $\beta = 0{\cdot}01$ (lower). Bottom: experimental results for $\beta = 0{\cdot}06$

totally occupied by the inner circulatory streaming for the experimental case. The numerical case that compares very well with the experimental one is for $\beta = 0{\cdot}1$. For this case too, the flow field around the body is almost occupied by the inner circulatory streaming. The pair of vortices above the body (and below by symmetry) are located almost symmetrically about the y-axis with the vortex on the cuspidal edge of the profile occupying a slightly larger portion of the domain. As β is increased, the asymmetry of the location of the vortices becomes more pronounced. At $\beta = 0{\cdot}06$, the same as the experiment, the numerical steady streamlines show that the vortex on the obtuse edge occupies a larger portion of the plotted domain and the vortex on the cuspidal edge has shrunk. At $\beta = 0{\cdot}1$, the vortex, which was on the obtuse edge for $\beta = 0{\cdot}06$, has now shifted its location towards the cuspidal edge and completely occupies the second vortex, which itself has shrunk even more. The numerical result for $\beta = 0{\cdot}1$ compares very well with the experiment for $\beta = 0{\cdot}06$. Overall, the numerical results show the characteristics of the experimental flow.

The example in Figure 21 shows the steady streamlines for the numerical case at seven different values of β and for the experimental case at four different values of β, all for a moderate value of R_ω of 206. The numerical results are for values of β of 0·0091, 0·0131, 0·0188, 0·0251, 0·0325, 0·0622 and

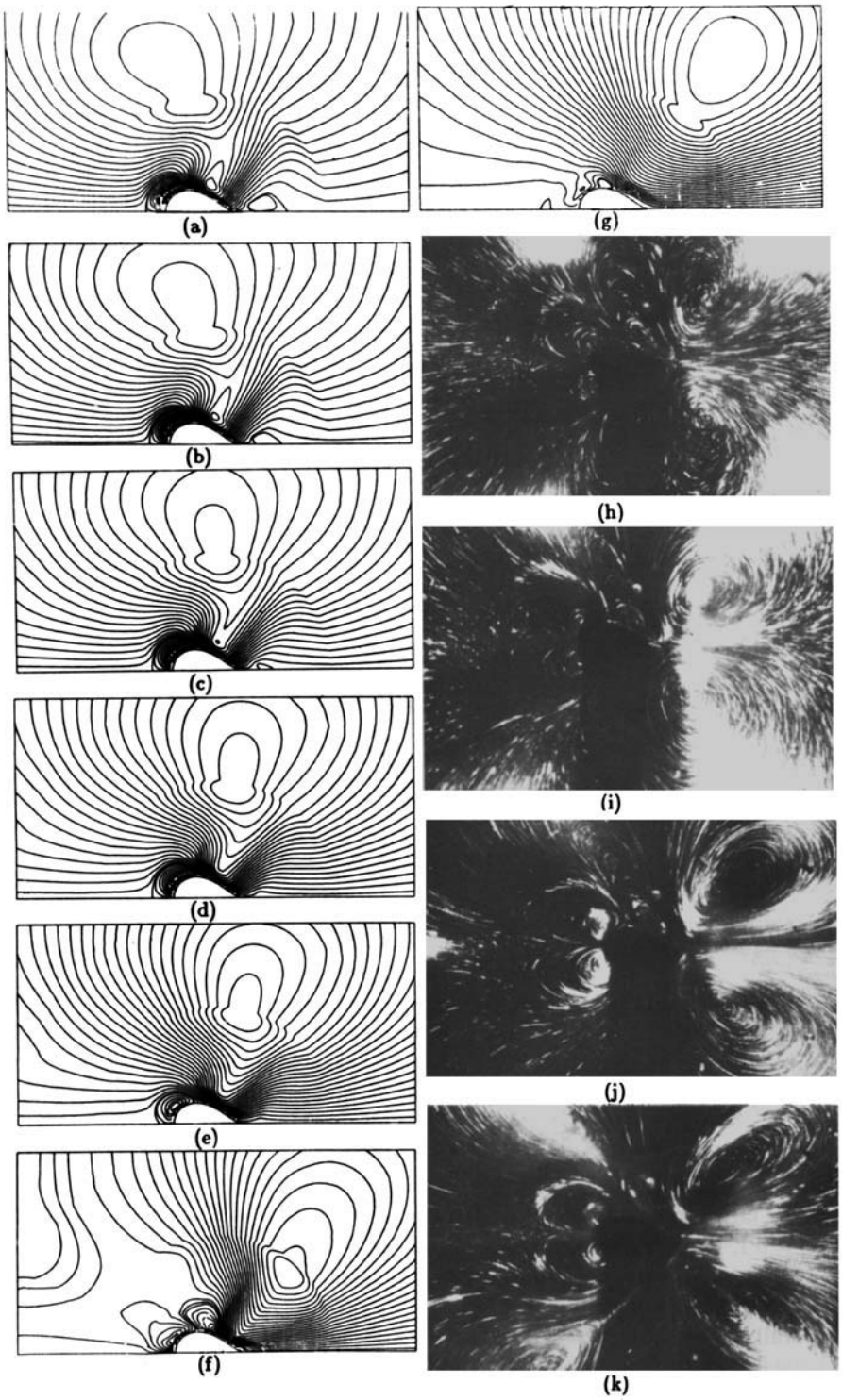

Figure 21. Steady streamlines for oscillating Joukowski profile for $R_\omega = 206$, $D_0/b = 18{\cdot}3$: (a) $\beta = 0{\cdot}0091$, (b) $\beta = 0{\cdot}0131$, (c) $\beta = 0{\cdot}0188$, (d) $\beta = 0{\cdot}0251$, (e) $\beta = 0{\cdot}0325$, (f) $\beta = 0{\cdot}0622$, (g) $\beta = 0{\cdot}1$, (h) $\beta = 0{\cdot}0091$, (i) $\beta = 0{\cdot}0131$, (j) $\beta = 0{\cdot}0251$, (k) $\beta = 0{\cdot}0457$

Table XI. Maximum and minimum steady stream function for oscillating Joukowski profile

R_ω	β	Location of minimum stream function		Minimum steady stream function	Location of maximum stream function		Maximum steady stream function
		x	y		x	y	
55·1	0·01	−0·7	0·35	−0·0015	0·05	0·425	0·0016
55·1	0·064	−1·15	1·05	−0·0341	−0·05	0·325	0·0138
55·1	0·1	0·7	2·275	−0·0469	−0·25	0·375	0·0047
206	0·0091	−0·6	0·275	−0·0013	−0·2	1·575	0·0018
206	0·0131	−0·6	0·275	−0·0182	−0·05	1·575	0·0029
206	0·0188	−0·06	0·275	−0·002686	0·05	1·575	0·005125
206	0·0251	−0·6	2·275	−0·0037	0·25	1·575	0·0096
206	0·0325	−0·6	0·275	−0·0049	0·4	1·575	0·0234
206	0·0622	1·05	1·125	−0·0337	−0·05	0·3	0·0112
206	0·1	1·5	2·125	−0·1205	−0·25	0·35	0·0049

0·1 and the experimental results are for values of β of 0·0091, 0·0131, 0·251 and 0·0457. The experimental results show a more complicated flow pattern for small values of β. At $\beta = 0{\cdot}0091$, it is observed that there are three pairs of vortices very close to the body. Two of them are located adjacent to the body, whereas the third one is located further away in the flow field on the cuspidal edge. As the value of β is increased, it is observed that the central vortex shrinks and the vortex on the cuspidal edge becomes more dominant, and at $\beta = 0{\cdot}0457$ the central vortex has almost disappeared. In all the experimental results shown, the vortex on the obtuse edge remains essentially at the same location. The numerical result at $\beta = 0{\cdot}0091$ shows three main vortices, two of which are located adjacent to the body, whereas the third one is located further away in the flow field. As the value of β is increased the vortex adjacent to the body and close to the cuspidal edge shrinks and the vortex further away in the flow field becomes more dominant and moves towards the cuspidal edge. At $\beta = 0{\cdot}0251$ and $\beta = 0{\cdot}0325$ the vortex adjacent to the body and close to the cuspidal edge has disappeared and the vortex further away in the flow field has moved to the cuspidal edge. For all values of β from 0·0091 to 0·0325, the vortex adjacent to the body and close to the obtuse edge remains at essentially the same location.

The numerical results for $R_\omega = 206$ and $\beta = 0{\cdot}0457$ did not converge even when the converged results for $R_\omega = 206$ and two separate values of β of 0·0325 and 0·0622 were used as initial guess solutions. This may indicate a change in flow pattern, which is indeed seen at $\beta = 0{\cdot}0622$. In this case, again three vortices appear with two vortices located close to the obtuse edge and tightly packed adjacent to the body, whereas the third one spreads more into the flow field and is located at a cuspidal edge. As β is increased to 0·1, the vortices located close to the body shrink and the vortex on the cuspidal edge becomes more dominant and spreads over the whole plotted domain. Unfortunately, the experimental results at higher values of β are not available to observe the existence of a critical value of β for transition to a different flow pattern. Overall, the numerical results exhibit the trends observed experimentally.

The steady flow components illustrated in these Figures are again expected to be small compared to the main periodic flow. The actual maxima of the resultant velocities and their locations in the flow domain are shown in Table XII. These maximum velocities were obtained only from a check of nodal values, so they may not be the global maxima. In all cases, except for $R_\omega = 55{\cdot}1$ and $\beta = 0{\cdot}1$, the maximum velocity occurred at the body mean position. For the

Table XII. Maximum steady component of velocity for oscillating Joukowski profile.

R_ω	β	Location of maximum steady velocity		$\frac{u_{max}}{u_0}$
		x	y	
55·1	0·01	−0·05105	0·2313	0·0407
55·1	0·064	−0·0567	0·2466	0·6910
55·1	0·1	−0·7	0	0·5134
206	0·0091	−0·5105	0·2313	0·0582
206	0·0131	−0·5105	0·2313	0·0839
206	0·0188	−0·5105	0·2313	0·1206
206	0·0251	−0·5105	0·2313	0·1610
206	0·0325	0·1134	0·1431	0·3073
206	0·0622	0·1134	0·1431	0·8377
206	0·1	−0·5105	0·2313	0·5473

aforementioned case, the maximum steady velocity occurs at a position very close to the body mean position.

Some of the results from equation (38) are shown in Figures 22, 23 and 24. The results for $R_\omega = 55{\cdot}1$ are shown in Figures 22 and 23 for values of β of 0·01 and 0·1, respectively, and the results for $R_\omega = 206$ and $\beta = 0{\cdot}1$ are shown in Figure 24. These Figures show velocity vectors over a uniform mesh in the vicinity of the body for $t = 0$, $\pi/4$, $\pi/2$, $3\pi/4\pi$, $5\pi/4$, $3\pi/2$ and $7\pi/4$, that is equal time steps over one full cycle of body motion. Unlike the case of the square and the circular body, where it is necessary to show the results only for one half cycle of body motion because of the symmetry, the results for the Joukowski profile have to be shown for one full cycle. The size of each vector indicates the velocity magnitude. Note that the scale in each illustration is different.

It is clear from these Figures that there is one main vortex in the upper half of the fluid flow and although it does move slightly from side to side it is located just above (and below by symmetry) the oscillating body. For $R_\omega = 55{\cdot}1$ and values of β of 0·01 and 0·1 the location of the main vortex is essentially the same. As R_ω is increased to 206, this vortex system moves closer to the body and decreases in size, thereby increasing the velocity gradients in that region. Consequently, the boundary layer thickness is also decreased.

The results for the stability analysis are obtained by using the finite element grid in Figure 19 with $D_0/b = 18{\cdot}3$. This grid has 62 pressure variables and 256 velocity variables for both symmetric and antisymmetric modes.

The stability analysis is performed for the oscillating Joukowski profile for $R_\omega = 206$ and $\beta = 0{\cdot}0251$. The results for the top 135 eigenvalues in descending order of magnitude are presented in Tables XIII and XIV for the symmetric and antisymmetric perturbation modes, respectively. The flow situation considered here is very close to the flow situation with the same values of R_ω of 206 and β of 0·0457, where the numerical solution did not converge. The results show that there are 124 eigenvalues (twice the number of pressure variables) with magnitude equal to 1 and the rest are all less than 1. This indicates that the steady-state solution is stable for both symmetric and antisymmetric modes. The results also show that the eigenvalues have essentially converged at $\Delta t = 2\pi/10$ and further reduction of the time step interval to $\Delta t = 2\pi/40$ brings about no change

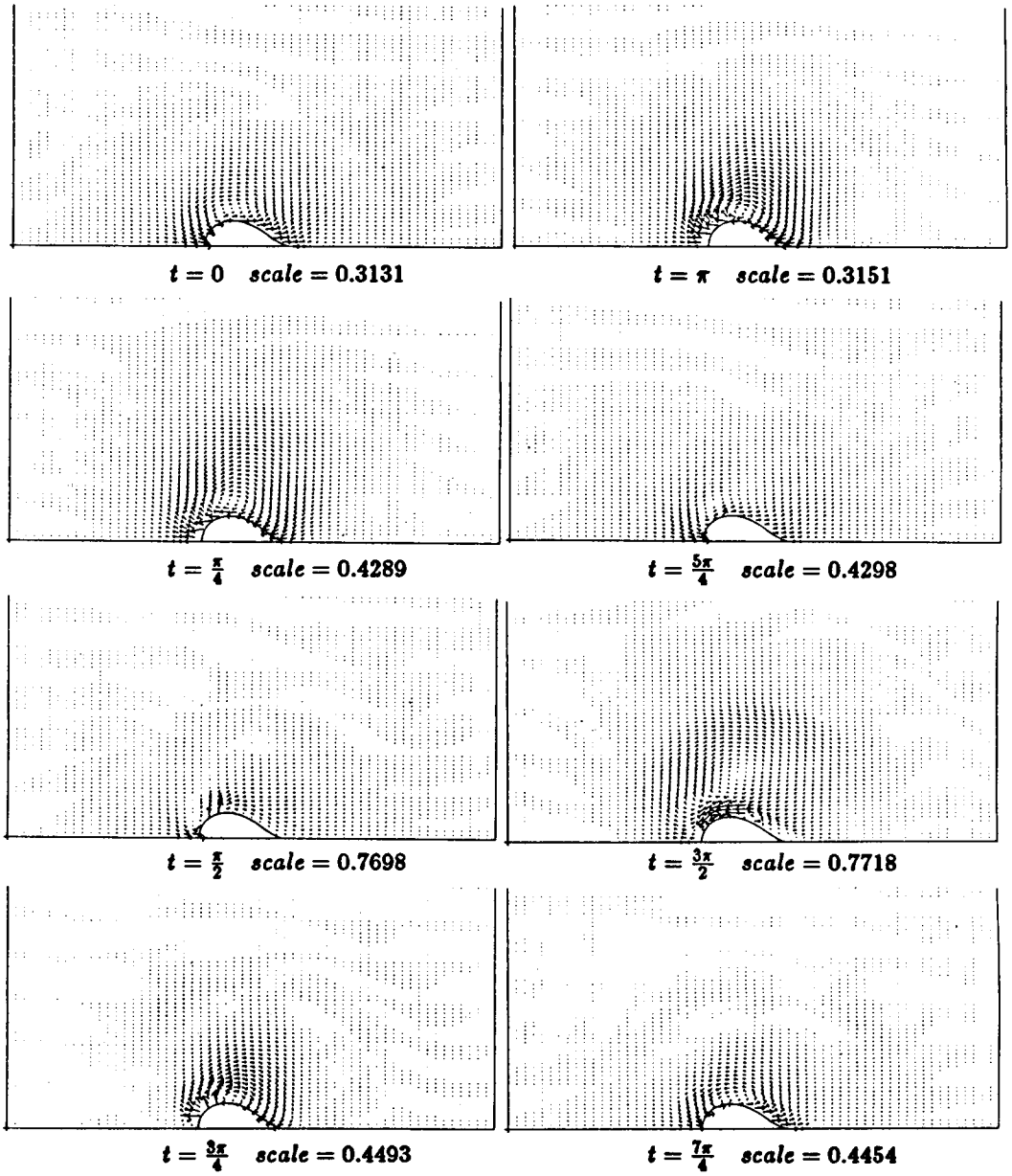

Figure 22. Velocity vectors for oscillating Joukowski profile: $R_\omega = 55{\cdot}1$, $\beta = 0{\cdot}01$, $D_0/b = 18{\cdot}3$

in them. Many of the eigenvalues in the present case have magnitudes close to 1, which qualitatively indicates a 'weakly' stable situation. This may be due to the fact that the flow under consideration is very close to the flow for which the numerical results did not converge.

4. CONCLUDING REMARKS

The present method of representing the interaction between a solid body and viscous flow seems to

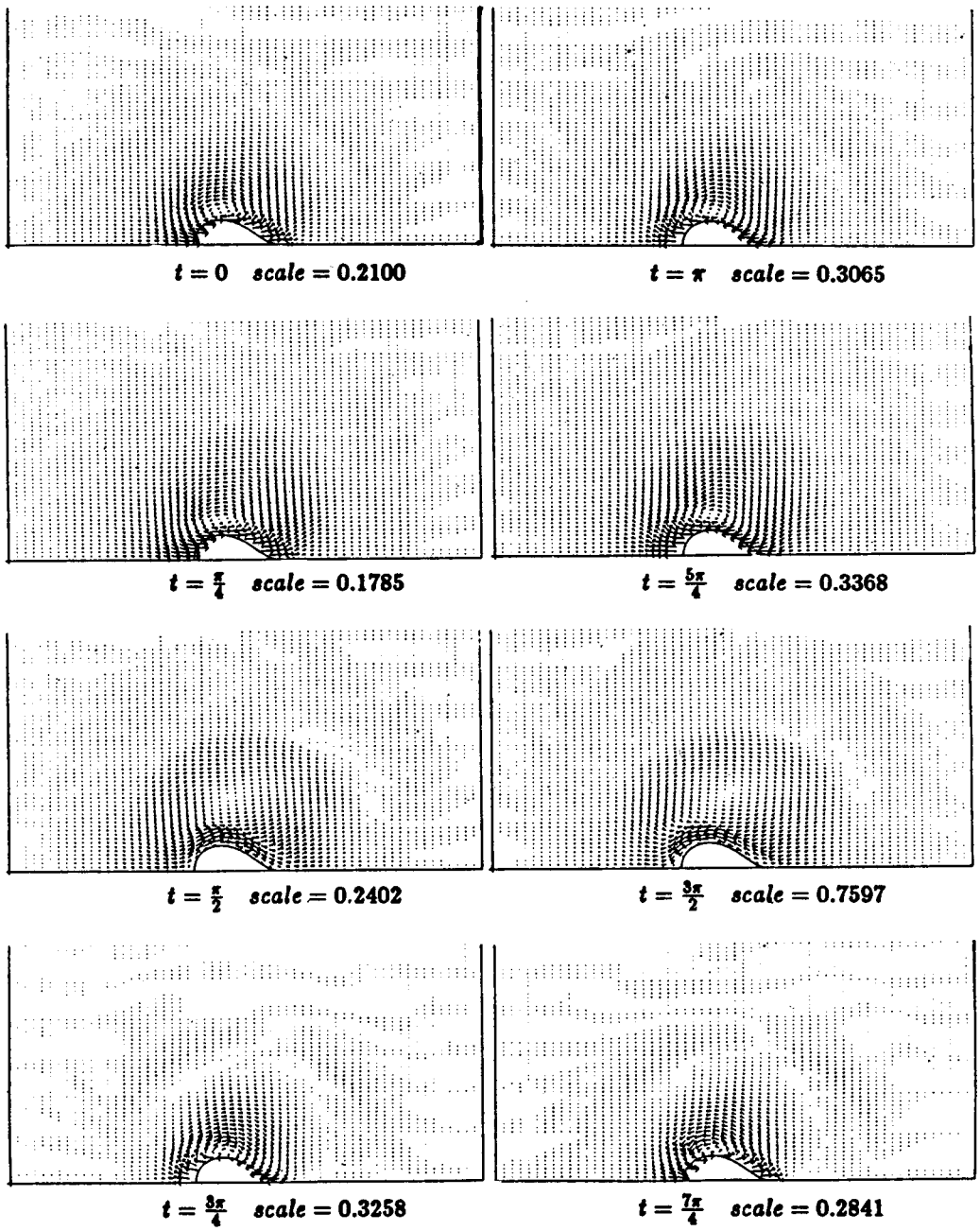

Figure 23. Velocity vectors for oscillating Joukowski profile: $R_\omega = 55{\cdot}1$, $\beta = 0{\cdot}1$, $D_0/b = 18{\cdot}3$

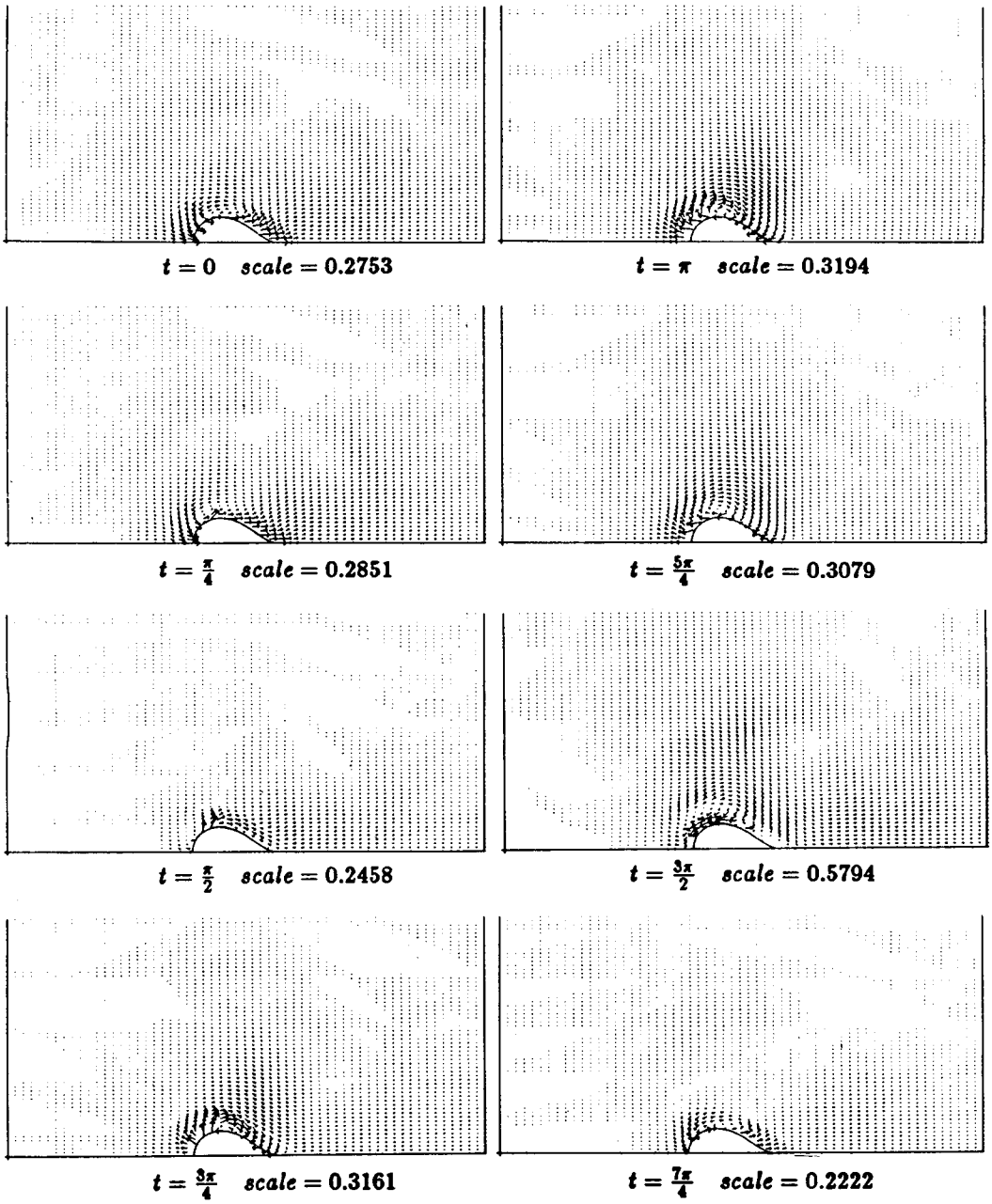

Figure 24. Velocity vectors for oscillating Joukowski profile: $R_\omega = 206$, $\beta = 0{\cdot}1$, $D_0/b = 18{\cdot}3$

Table XIII. Symmetric mode stability analysis for oscillating Joukowski profile: $R_\omega = 206$, $\beta = 0{\cdot}0251$

Eigenvalue no.	$\Delta t = \frac{2\pi}{10}$	$\Delta t = \frac{2\pi}{40}$
	$\lvert\lambda\rvert$	$\lvert\lambda\rvert$
1	1	1
2	1	1
3	1	1
.	.	.
.	.	.
.	.	.
124	1	1
125	0·98638	0·98638
126	0·98478	0·98478
127	0·97876	0·97876
128	0·97069	0·97069
129	0·96840	0·96840
130	0·96319	0·96319
131	0·96020	0·96020
132	0·95102	0·95102
133	0·94683	0·94683
134	0·93428	0·93428
135	0·93314	0·93314

Table XIV. Antisymmetric mode stability analysis for oscillating Joukowski profile: $R_\omega = 206$, $\beta = 0{\cdot}0251$

Eigenvalue no.	$\Delta t = \frac{2\pi}{10}$	$\Delta t = \frac{2\pi}{40}$
	$\lvert\lambda\rvert$	$\lvert\lambda\rvert$
1	1	1
2	1	1
3	1	1
.	.	.
.	.	.
.	.	.
124	1	1
125	0·99460	0·99460
126	0·98569	0·98569
127	0·98478	0·98478
128	0·98154	0·98154
129	0·97874	0·97874
130	0·97059	0·97059
131	0·96721	0·96721
132	0·96319	0·96319
133	0·96045	0·96045
134	0·95995	0·95995
135	0·95067	0·95067

work very well. In particular, the Taylor series expansion of the oscillating body boundary conditions with respect to the fixed finite element grid is apparently adequate to capture the basic non-linear phenomena of secondary flow.

The full non-linear Newton–Raphson procedure for solving the non-linear algebraic equations is successful for the range of parameters considered in the present study.

The overall agreement between the numerical and the experimental results for the basic non-linear phenomena of steady streaming is very good. The results for the instantaneous velocity vectors in the fluid domain show one main vortex in the upper half (and lower half by symmetry) of the transient flow. As the frequency Reynolds number R_ω increases, this vortex moves closer to the body and decreases in size, thereby increasing the velocity gradients in that region. This indicates that the boundary layer thickness decreases with the increasing R_ω, as it should.

Overall, the implicit numerical integration scheme using the trapezoidal rule to obtain the transition matrix for stability analysis seems to work very well. The convergence to the transition matrix and thereby to the eigenvalues is obtained by increasing the number of time steps (that is, decreasing the time step interval). The scheme is unconditionally stable with respect to the size of the time step. The computer time required for obtaining the converged results is very high because the number of matrix inversions required are equal to the number of time steps. Therefore, any increase in the number of time steps would correspond to a substantial increase in the computer time required.

ACKNOWLEDGEMENT

This work has been supported by the Canadian Natural Sciences and Engineering Research Council. The authors are indebted to M. Tatsuno for sending original photographs from his experiments.

APPENDIX I

The net global u and v degrees of freedom for finite element discretization of viscous fluid each number n, including r degrees of freedom at the interface between the finite element grid and the mean position of the moving body. There are m net global p degrees of freedom. Also the u and v degrees of freedom at the edge of an element which is at the interface between the viscous fluid and the mean position of the body each number q. Therefore, we can write the matrices in equation (10) as

$$\mathbf{P} = -\begin{bmatrix} \sum_{l=n-r+1}^{n} M_{il}^{uu} C_{lj} & 0 & 0 \\ 0 & \sum_{l=n-r+1}^{n} M_{il}^{vv} C_{lj} & 0 \\ 0 & 0 & 0 \end{bmatrix},$$

$$\mathbf{Q} = \mathbf{P} + \begin{bmatrix} \sum_{m=n-r+1}^{n} (\delta_{ijm}^{x} + \delta_{imj}^{x}) & \sum_{m=n-r+1}^{n} \delta_{ijm}^{y} & 0 \\ 0 & \sum_{m=n-r+1}^{n} \delta_{imj}^{x} & 0 \\ 0 & 0 & 0 \end{bmatrix},$$

$$\mathbf{R} = -\frac{1}{R_\omega}\begin{bmatrix} \sum_{l=n-r+1}^{n} K_{il}^{uu} C_{ij} & \sum_{l=n-r+1}^{n} K_{il}^{uv} C_{ij} & 0 \\ \sum_{l=n-r+1}^{n} K_{li}^{uv} C_{lj} & \sum_{l=n-r+1}^{n} K_{il}^{vv} C_{lj} & 0 \\ -\sum_{l=n-r+1}^{n} P_{li}^{x} C_{lj} & -\sum_{l=n-r+1}^{n} P_{li}^{y} C_{lj} & 0 \end{bmatrix},$$

$$\mathbf{F} = \begin{Bmatrix} \sum_{j=n-r+1}^{n} M_{ij}^{uu} \\ 0 \\ 0 \end{Bmatrix},$$

$$\mathbf{G} = -\frac{1}{R_\omega}\begin{Bmatrix} \sum_{j=n-r+1}^{n} K_{ij}^{uu} \\ \sum_{j=n-r+1}^{n} K_{ji}^{uv} \\ -\sum_{j=n-r+1}^{n} P_{ji}^{x} \end{Bmatrix},$$

$$\mathbf{H} = \begin{Bmatrix} \sum_{l=n-r+1}^{n} M_{il}^{uu} \sum_{j=1}^{q} C_{lj} - \sum_{j=n-r+1}^{n} \sum_{k=n-r+1}^{n} \delta_{ijk}^{x} \\ 0 \\ 0 \end{Bmatrix},$$

$$\mathbf{L} = \frac{1}{R_\omega}\begin{Bmatrix} \sum_{l=n-r+1}^{n} K_{il}^{uu} \sum_{j=1}^{q} C_{lj} \\ \sum_{l=n-r+1}^{n} K_{li}^{uv} \sum_{j=1}^{q} C_{lj} \\ -\sum_{l=n-r+1}^{n} P_{li}^{x} \sum_{j=1}^{q} C_{lj} \end{Bmatrix},$$

$$\mathbf{J} = -\begin{Bmatrix} \sum_{l=n-r+1}^{n} M_{il}^{uu} \sum_{j=1}^{q} C_{lj} \\ 0 \\ 0 \end{Bmatrix}.$$

APPENDIX II

The matrix $\mathbf{Z}(t)$ in equation (18) is given by

$$\mathbf{Z}(t) = \mathbf{K} + \beta\begin{bmatrix} \delta_{imj}^{y} v_m + \delta_{imj}^{x} u_m + \delta_{ijm}^{x} u_m & \delta_{ijm}^{y} u_m & 0 \\ \delta_{ijm}^{x} v_m & \delta_{imj}^{x} u_m + \delta_{imj}^{y} v_m + \delta_{ijm}^{y} v_m & 0 \\ 0 & 0 & 0 \end{bmatrix}$$

REFERENCES

1. Harry Armen and S. Stiansen, (eds), *Computational Methods for Offshore Structures (Symposium)*, ASME, AMD V. 37, 1980.
2. T. Belytschko and J. M. Kennedy, 'Computer models for sub-assembly simulation', *Nucl. Eng. Des.*, **49**, 17–38 (1978).
3. W. K. Liu, 'Finite element procedures for fluid–structure interactions and applications to liquid storage tanks', *Nucl. Eng. Des.*, **65**(2), 221–238 (1982).
4. M. D. Olson and P. G. Pattani, 'Nonlinear analysis of rigid body–viscous flow interaction', *5th Symposium on Finite Element Methods in Flow Problems*, Austin, Texas, 1984; also in R. H. Gallagher, G. F. Carey, J. T. Oden and O. C. Zienkiewicz (eds), *Finite Element in Fluids, Vol. 6*, Wiley, 1985.
5. P. G. Pattani and M. D. Olson, 'Stability of nonlinear solutions of rigid body–viscous flow interaction', *4th Int. Conf. on Num. Methods in Laminar and Turbulent Flow*, Swansea, 8–13, July 1985.
6. P. G. Pattani, 'Nonlinear analysis of rigid body–viscous flow interaction', *Ph.D. Thesis*, Department of Civil Engineering, University of British Columbia, Vancouver, Canada, 1986.
7. N. W. McLachlan, *Ordinary Non-Linear Differential Equations in Engineering and Physical Sciences*, second edn, The Clarendon Press, Oxford, 1958.
8. H. Schlichting, *Boundary Layer Theory*, 6th edn, McGraw-Hill, 1968.
9. A. H. Nayfeh and D. T. Mook, *Nonlinear Oscillations*, Wiley, New York, 1979.
10. P. Friedmann, C. E. Hammond and T. H. Woo, 'Efficient numerical treatment of periodic systems with application to stability problems', *Int. j. numer. methods eng.*, **11**, 1117–1136 (1977).
11. T. J. R. Hughes, 'Analysis of transient algorithms with particular reference to stability behaviour', in T. J. R. Hughes and T. Belytschko (eds), *Computational Methods for Transient Analysis, Vol. 1*, North-Holland, 1983.
12. M. Tatsuno, 'Circulatory streaming in the vicinity of an oscillating square cylinder', *J. Physical Soc. Japan*, **36**(4), 1185–1191 (1974).
13. M. Tatsuno, 'Circulatory streaming around an oscillating circular cylinder at low Reynolds numbers', *J. Physical Soc. Japan*, **35**(3), 915–920 (1973).
14. M. Tatsuno, 'Secondary flow around oscillating assymetric cylinders', *Reports of Research Institute of Applied Mechanics, Kyushu University*, **XXVIII**, (89), 35–47 (1980).